

**HYDROGEN ADSORPTION ON NICKEL SUPPORTED  
ON ACTIVATED CARBON NANOFIBERS**

**NATTHAPORN THAWEELAP**



**A Thesis Submitted in Partial Fulfillment of the Requirements for the  
Degree of Master of Science in Chemistry  
Suranaree University of Technology  
Academic Year 2019**

# การดูดซับไอโครเจนบนเส้นใยคาร์บอนระดับนาโนเมตรที่ติดด้วยโลหะนิกเกิล



นางสาวณัฐพร ทวีลาภ

วิทยานิพนธ์นี้เป็นส่วนหนึ่งของการศึกษาตามหลักสูตรปริญญาวิทยาศาสตรมหาบัณฑิต

สาขาวิชาเคมี

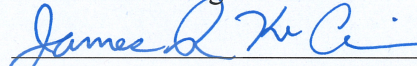
มหาวิทยาลัยเทคโนโลยีสุรนารี

ปีการศึกษา 2562

**HYDROGEN ADSORPTION ON NICKEL SUPPORTED ON  
ACTIVATED CARBON NANOFIBERS**

Suranaree University of Technology has approved this thesis submitted in partial fulfillment of the requirements for a Master's Degree.

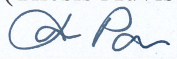
Thesis Examining Committee

  
(Prof. Dr. James Ketudat-Cairns)

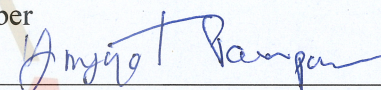
Chairperson

  
(Assoc. Prof. Dr. Rapee Utke)

Member (Thesis Advisor)

  
(Dr. Autchara Pangon)

Member

  
(Dr. Yingyot Poo-arporn)

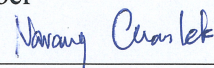
Member

  
(Asst. Prof. Dr. Suwit Suthirakun)

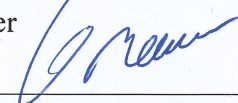
Member

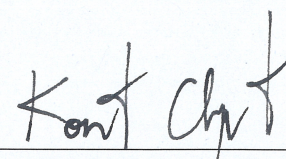
  
(Dr. Ittipon Fongkaew)

Member

  
(Dr. Narong Chanlek)

Member

  
(Assoc. Prof. Dr. Worawat Meevasana)

  
(Assoc. Prof. Flt. Lt. Dr. Kontorn Chamniprasart)

Vice Rector for Academic Affairs  
and Internationalization

Dean of Institute of Science

ณัฐพร ทวีลาภ : การดูดซับไฮโดรเจนบนเส้นใยคาร์บอนระดับนาโนที่ติดด้วยโลหะ  
นิกเกิล (HYDROGEN ADSORPTION ON NICKEL SUPPORTED ON ACTIVATED  
CARBON NANOFIBERS) อาจารย์ที่ปรึกษา : รองศาสตราจารย์ ดร.ระพี อุทเคอ,  
59 หน้า.

การแตกตัวการดูดซับ/ การกักเก็บไฮโดรเจน/ การติดโลหะบนคาร์บอน/ ความสามารถในการ  
ผันกลับของการกักเก็บไฮโดรเจน / การสร้างแบบจำลองทางคอมพิวเตอร์/ การคำนวณแบบเฟสส์  
พรีนซิเพิล

ในวิทยานิพนธ์นี้ เส้นใยคาร์บอนระดับนาโน (ACNF/PVP) ที่เตรียมโดยวิธีการคาร์บอน  
ไนซ์และการกระตุ้นทางเคมีของโพลีอะคริโลไนไตรล์ (PAN)-โพลีไวนิลไพโรลิโดน(PVP) นาโน  
ไฟเบอร์ และเจือด้วย 5-20 wt. % นิลเกิลถูกเสนอสำหรับการดูดซับไฮโดรเจนที่อุณหภูมิห้อง  
ความสามารถในการดูดซับไฮโดรเจนสูงสุดถึง 2.12 wt. %  $H_2$  ภายใต้ความดันไฮโดรเจน 100 บาร์  
และความสามารถในการกักเก็บเมื่อครบ 10 รอบ มีความจุเฉลี่ย 1.17 wt. %  $H_2$  ภายใต้ความดัน  
ไฮโดรเจน 50 บาร์ ถูกพบจากตัวอย่าง 5Ni-ACNF/PVP การคำนวณทางคอมพิวเตอร์และการ  
ทดลองยืนยันปฏิกิริยาระหว่างนิกเกิลและอะตอมไฮโดรเจน ( $E_b = 826 \text{ kJ/mol}$ ) ซึ่งนำไปสู่การกระจาย  
ตัวที่ดีของอนุภาคนิกเกิลระดับนาโน ผลลัพธ์นี้ช่วยเพิ่มพื้นที่ผิวของปฏิกิริยาสำหรับการดูดซับ  
ไฮโดรเจนและป้องกันการรวมตัวของอนุภาคนิกเกิลเมื่อการกักเก็บไฮโดรเจน 10 รอบ พลังงานการ  
ดูดซับที่คำนวณได้คือ  $-88 \text{ kJ/mol } H_2$  แสดงถึงลักษณะการดูดซับทางเคมีที่แข็งแรง โดยมีระยะ  
พันธะนิกเกิลกับไฮโดรเจนเฉลี่ย 1.71 อังสตรอม ยิ่งไปกว่านั้นผลการคำนวณประจักษ์ระบุว่า โลหะ  
นิกเกิลแบ่งปันอิเล็กตรอนให้กับไฮโดรเจนเพื่อสร้างพันธะนิกเกิล-ไฮโดรเจน (Ni-H) เนื่องจาก  
ไฮโดรเจนมีค่าอิเล็กโตรเนกาติวิตีมากขึ้น นอกจากนี้กลไกการดูดซับไฮโดรเจนไม่ได้เป็นเพียงการ  
ดูดซับทางเคมีของอะตอมไฮโดรเจนที่ดูดซับไปยังอนุภาคนาโนของ Ni เท่านั้น แต่ยังรวมถึงการดูด  
ซับทางกายภาพและการรั่วไหลของไฮโดรเจนอีกด้วย ดังนั้นประสิทธิภาพการดูดซับไฮโดรเจนจึง  
สามารถปรับปรุงได้โดยการเพิ่มพื้นที่ผิว และการกระจายตัวของอนุภาคนิกเกิลระดับนาโนบน  
พื้นผิวคาร์บอน

สาขาวิชาเคมี  
ปีการศึกษา 2562

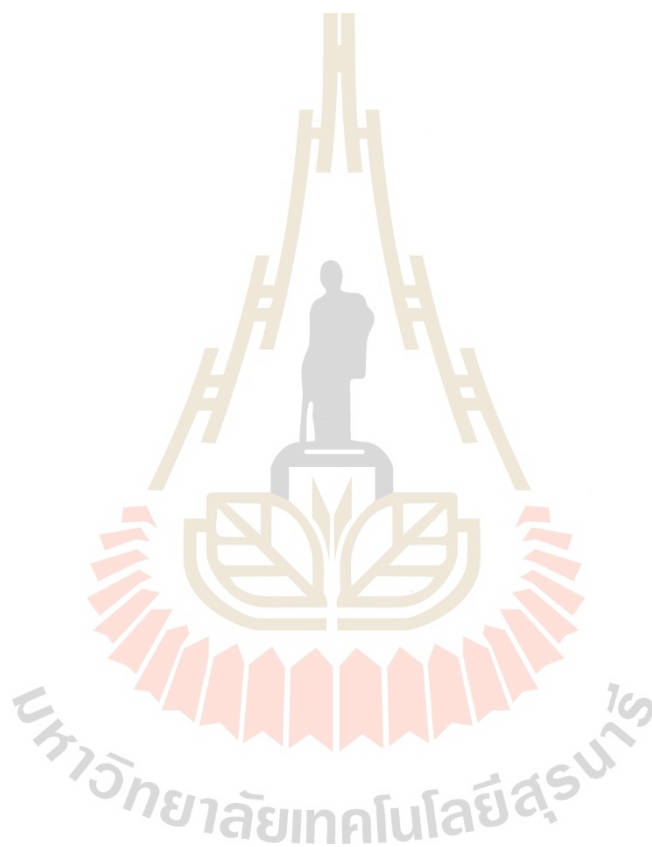
ลงมือชื่อนักศึกษา ณัฐพร ทวีลาภ  
ลงมือชื่ออาจารย์ที่ปรึกษา ดร.ระพี อุทเคอ

NATTHAPORN THAWEELAP : HYDROGEN ADSORPTION ON  
NICKEL SUPPORTED ON ACTIVATED CARBON NANOFIBERS.  
THESIS ADVISOR : ASSOC. PROF. RAPEE UTKE, Ph.D. 59 PP.

DISSOCIATIVE ADSORPTION/ HYDROGEN STORAGE/METAL DOPED  
CARBON/ REVERSIBILITY/ DFT CALCULATION/ FIRST-PRINCIPLE  
COMPUTATIONS.

In this thesis, activated carbon nanofibers (ACNF/PVP) prepared by carbonization and chemical activation of polyacrylonitrile (PAN)-polyvinylpyrrolidone (PVP) electrospun nanofibers and doped with 5-20 wt. % Ni are proposed for hydrogen adsorption at room temperature. The excellent hydrogen adsorption capacities of up to 2.12 wt. % H<sub>2</sub> (p(H<sub>2</sub>)=100 bar) and cycling stability upon 10 cycles with average capacity of 1.17 wt. % H<sub>2</sub> (p(H<sub>2</sub>)=50 bar) are obtained from 5Ni-ACNF/PVP. Computations and experiments confirm strong interactions between Ni and heteroatoms ( $E_b=826$  kJ/mol), leading to good distribution of Ni nanoparticles. The latter results enhance reactive surface area for hydrogen adsorption and preventing agglomeration of Ni particles upon cycling. The calculated adsorption energy of -88 kJ/mol H<sub>2</sub> implies strong chemisorption character with an average Ni-H bond distance of 1.71 Å. Furthermore, The Bader charge indicated Ni shared its electrons to H to form Ni-H bonds due to greater electronegativity of H. Besides, hydrogen adsorption mechanisms are not only chemisorption of adsorbed hydrogen atoms onto Ni nanoparticles but also physisorption and spillover of hydrogen. Therefore, hydrogen adsorption performance could be improved by the enhanced

reactive surface area and uniform distribution of Ni nanoparticles on the carbon surface.



School of Chemistry

Academic Year 2019

Student's Signature ศศิพัชร ทวีลาภ

Advisor's Signature Rayne Othe

## **ACKNOWLEDGEMENTS**

I would like to express my sincere thanks to several people who help me to complete my thesis and thereby allowing me to reach my goal of achieving a M. Sc.

First of all, I would like to thank my thesis advisor, Assoc. Prof. Dr. Rapee Utke for her invaluable help and constant encouragement throughout the course of this research. I am most grateful for her teaching and advice, not only the research methodologies but also many other methodologies in life. I would not have achieved this much and this thesis would not have been completed without all the support that I have always received from her.

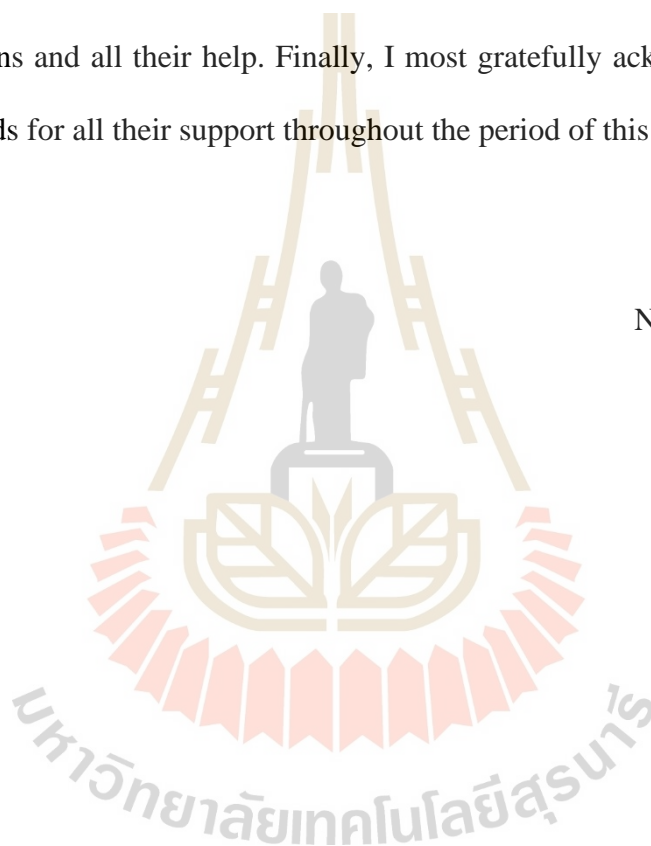
I would like to thank my thesis Co-advisor Dr. Autchara Pangon (National Nanotechnology Center (NANOTEC), National Science and Technology Development Agency (NSTDA), Pathum Thani 12120, Thailand), for giving me a chance to research work at NANOTEC. Under her supervision, she was kindly advising and helping me along with my thesis. I appreciate her kind support, suggestion, encouragement and discussion throughout my thesis.

I would like to thank Dr. Suwit Suthirakul (School of Chemistry, Institute of Science, Suranaree University of Technology, Nakhon Ratchasima 30000, Thailand) and Dr. Ittipon Fongkaew (School of Physics, Institute of Science, Suranaree University of Technology) for their valuable time on the calculations for my work and kind suggestions. Dr. Narong Chanlekand (SUT-NANOTEC-SLRI, BL 5.2: SUT-NANOTEC-SLRI, Synchrotron Light Research Institute (Public Organization),

Thailand) for technical help, suggestion and analysis for the X-ray photoelectron spectroscopy (XPS) technique. Dr. Yingyot Poo-arporn (BL2.2: TRXAS, Synchrotron Light Research Institute (SLRI), Thailand) is thanked for technical help, suggestions and analysis for the X-ray absorption spectroscopy (XAS) technique.

In addition, I am grateful for the teachers of School of Chemistry, thesis examining committee, including Prof. Dr. James Ketudat-Cairns, and other persons for suggestions and all their help. Finally, I most gratefully acknowledge my parents and my friends for all their support throughout the period of this research.

Natthaporn Thaweelap

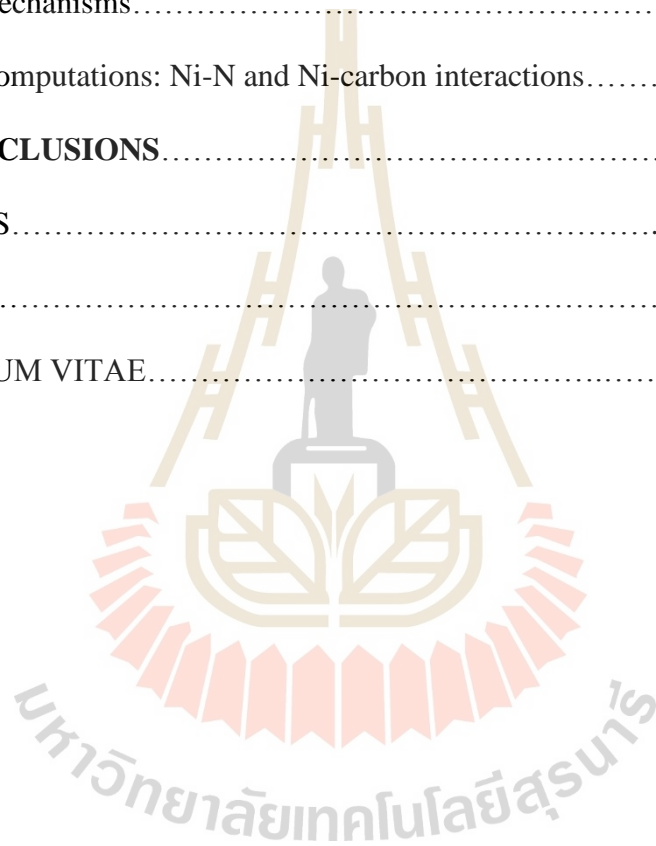


# CONTENTS

|  | <b>Page</b> |
|--|-------------|
| ABSTRACT IN THAI.....  | I           |
| ABSTRACT IN ENGLISH.....   | II          |
| ACKNOWLEDGEMENTS.....  | IV          |
| CONTENTS.....  | VI          |
| LIST OF FIGURES .....  | VIII        |
| LIST OF TABLES .....   | XI          |
| LIST OF ABBREVIATIONS.....                                       | XII         |
| <b>CHAPTER</b>   |             |
| <b>I INTRODUCTION.....</b>                                       | <b>1</b>    |
| <b>II LITERATURE REVIEWS.....</b>                                | <b>7</b>    |
| <b>III EXPERIMENTAL.....</b>                                     | <b>14</b>   |
| 3.1 Materials.....   | 14          |
| 3.2 Sample preparation.....                                      | 14          |
| 3.2.1 Preparation of activated carbon nanofibers.....            | 14          |
| 3.2.2 Preparation of Ni-doped ACNF-PVP.....                      | 15          |
| 3.3 Characterizations.....                                       | 16          |
| 3.4 Computations.....  | 21          |
| <b>IV RESULT AND DISCUSSIONS.....</b>                            | <b>22</b>   |
| 4.1 Morphology, textural parameters, and phase compositions..... | 22          |

## CONTENTS (Continued)

|  | <b>Page</b> |
|--|-------------|
| 4.2 Hydrogen adsorption performances and cycling stability.....                            | 27          |
| 4.3 Textural parameters, Ni-carbon interaction, and hydrogen adsorption<br>mechanisms..... | 30          |
| 4.4 Computations: Ni-N and Ni-carbon interactions.....                                     | 37          |
| <b>V CONCLUSIONS.....</b>  | <b>42</b>   |
| <b>REFERENCES.....</b>   | <b>44</b>   |
| <b>APPENDIX.....</b>   | <b>55</b>   |
| <b>CURRICULUM VITAE.....</b>   | <b>59</b>   |



## LIST OF FIGURES

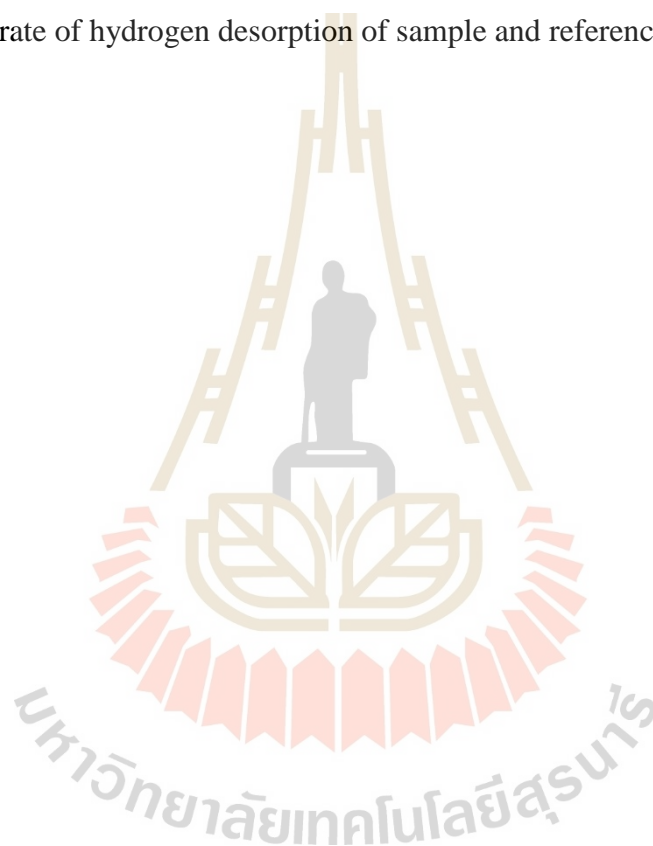
| Figure  | Page |
|---|------|
| 1.1 Travel distance and sizes of various vehicles.....  | 2    |
| 1.2 Physical- and material-based hydrogen storages.....   | 3    |
| 1.3 Hydrogen spillover mechanism.....   | 4    |
| 2.1 Porous carbon materials.....  | 7    |
| 2.2 FE-SEM images with different magnifications of N-doped CX.....  | 9    |
| 2.3 N <sub>2</sub> adsorption-desorption isotherms of the CNTs and Ni-doped CNTs.....                                       | 10   |
| 2.4 Hydrogen adsorption isotherms of the ACNFs and ACNFs-Ni at 303 K<br>up to 100 bar H <sub>2</sub> .....                  | 12   |
| 2.5 The relationship between Ni loading content and hydrogen adsorption<br>capacity of PCNF(A) and PCNF-Ni at 298 K(B)..... | 13   |
| 3.1 Components of hydrogen ad/desorption test station.....  | 20   |
| 4.1 SEM images of ACNF (A-B) and ACNF-PVP.....  | 23   |
| 4.2 SEM images of 5Ni-ACNF-PVP (a-d), 10Ni-ACNF-PVP (e-h) and<br>20Ni-ACNF-PVP (i-l).....                                   | 25   |
| 4.3 Raman spectra of ACNF-PVP, 5Ni-ACNF-PVP, 10Ni-ACNF-PVP,<br>and 20Ni-ACNF-PVP.....                                       | 26   |
| 4.4 PXD spectra of ACNF-PVP, 5Ni-ACNF-PVP, 10Ni-ACNF-PVP,<br>and 20Ni-ACNF-PVP.....   | 27   |

## LIST OF FIGURES (Continued)

| Figure | Page  |
|--------|---|
| 4.5    | Hydrogen adsorption of ACNF-PVP and Ni-doped ACNF-PVP (5-20 wt. %) at 25 °C under 50 bar H <sub>2</sub> for 5 h.....28  |
| 4.6    | Hydrogen adsorption at 25 °C under 20-100 bar H <sub>2</sub> of ACNF-PVP and 5Ni-doped ACNF-PVP (A) and cycling stability upon 10 ad/desorption cycles of 5Ni-doped ACNF-PVP (B).....29   |
| 4.7    | SEM images of 5Ni-doped ACNF-PVP after the 10 <sup>th</sup> desorption.....30   |
| 4.8    | N <sub>2</sub> adsorption isotherms (A) and pore size distribution (B) of ACNF-PVP and 5Ni-ACNF-PVP.....31  |
| 4.9    | FTIR spectra of ACNF-PVP and 5Ni-ACNF-PVP(A) and Chemical structure of PAN-based carbon nanofibers (B).....32   |
| 4.10   | C 1s (A), O 1s (B), and Ni 2p (C) XPS spectra of 5Ni-ACNF-PVP.....33  |
| 4.11   | In situ Ni K-edge XANES spectra during reduction (A) and hydrogen ad/desorption (B) of 5Ni-ACNF-PVP.....35  |
| 4.12   | The optimized structures of Ni <sub>13</sub> cluster on pyrrolic graphene in the absence (A) and presence (B) of hydrogen adsorption.....39   |
| 4.13   | The electron transfer is schematically depicted by the colors of each atom where the positive and negative values describe electron gains and losses, respectively. The labelled numbers represent the total number of electrons gain/loss by each atomic species. The H adsorbed structures at various |

**LIST OF FIGURES (Continued)**

| <b>Figure</b>  | <b>Page</b> |
|--|-------------|
| hydrogen coverages are used to simulate XANES spectra as compared with the experiment..... | 41          |
| A. Flow rate of hydrogen desorption of sample and reference.....                           | 57          |



## LIST OF TABLES

| Table | Page  |
|-------|---|
| 4.1   | Texture parameters of ACNF, ACNF-PVP, and 5Ni-ACNF/PVP.....24 |



## LIST OF ABBREVIATIONS

|                  |   |                    |
|------------------|---|--------------------|
| Å                | = | Angstrom           |
| °C               | = | degree celsius     |
| μ                | = | micrometer         |
| cm <sup>-1</sup> | = | wavenumber         |
| cm <sup>3</sup>  | = | cubic centimeter   |
| g                | = | gram               |
| h                | = | hour               |
| K                | = | kelvin             |
| kg               | = | kilogram           |
| kV               | = | kilo volt          |
| KeV              | = | kilo electron volt |
| L                | = | liter              |
| MW               | = | molecular weight   |
| mg               | = | milligram          |
| min              | = | minute             |
| m <sup>2</sup>   | = | square meter       |
| m <sup>3</sup>   | = | cubic meter        |
| mm               | = | millimeter         |
| ppm              | = | part per million   |
| s                | = | second             |

# CHAPTER I

## INTRODUCTION

The development of clean and renewable energy resources is of significant interest due to the increase of world pollution and energy consumption (Shafiee et al., 2009). Since one of the main sources of pollution is combustion engine, the demand of electric vehicles has been globally increased. Among various types of vehicles (Figure 1.1), fuel cell vehicles (FCVs) have drawn considerable attention due to its high energy efficiency. Proton exchange membrane fuel cell (PEMFC) is a promising technology for transportation because of its compact size, rapid startup due to low operating temperature and no release of any corrosive fluid hazards (Pollet et al., 2012). To use FCVs effectively, one of the key components is hydrogen storage system with high volumetric and gravimetric capacities (30 g H<sub>2</sub>/L system and 45 g H<sub>2</sub>/kg system, respectively) as well as moderate operating temperature and pressure (-40 to 85 °C and 5-12 bar H<sub>2</sub>) (U. S. Department of Energy, 2017).

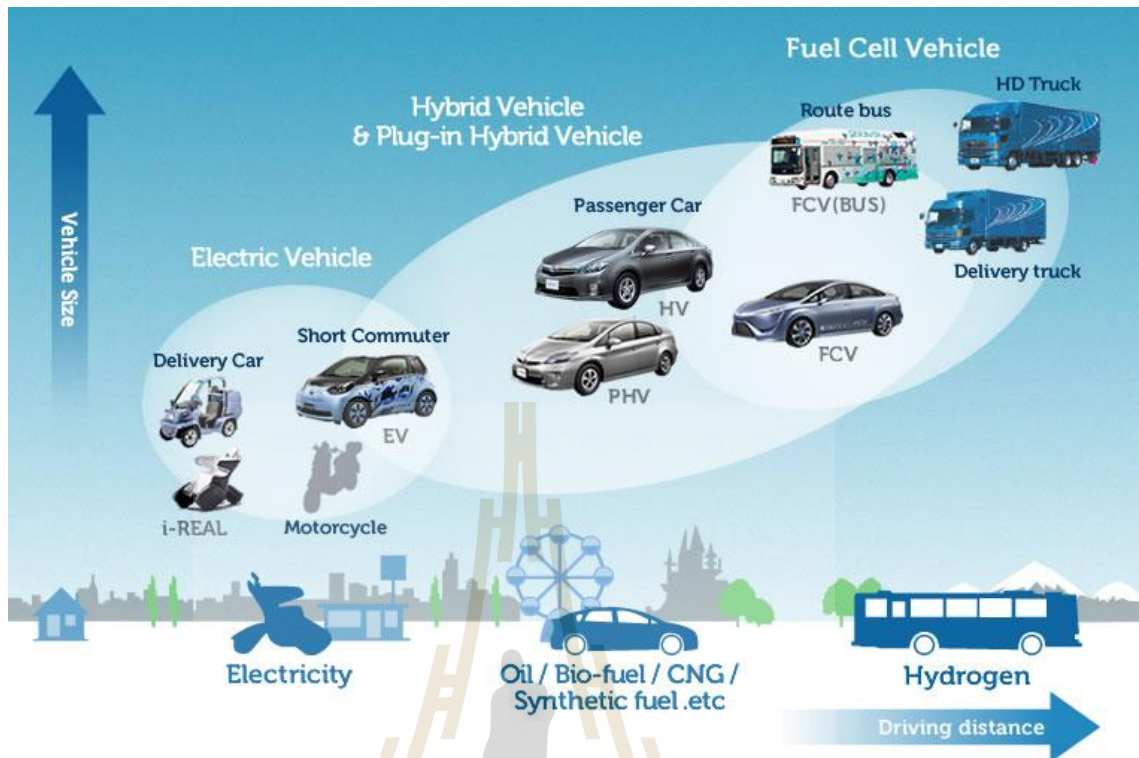


**Figure 1.1** Travel distance and sizes of various vehicles. (Toyota's Strategy for Environmental Technologies(online))

Hydrogen can be stored by physical- and material- based methods (Figure 1.2). For physical-based method, hydrogen is stored in the forms of compressed gas (up to 700 bar  $H_2$  at room temperature), cryo-compressed hydrogen (at  $-210\text{ }^\circ\text{C}$  under 350 bar  $H_2$ ), and liquefied hydrogen (at  $-253\text{ }^\circ\text{C}$ ). Materials with high tensile strength (compressed gas) and superior insulator (liquified  $H_2$ ) are required for hydrogen storage tank fabrication. In the case of material-based methods, hydrogen can be stored by chemical absorption in hydrides and physisorption in porous adsorbents. Although hydride materials own high theoretical volumetric and gravimetric capacities ( $70\text{-}150\text{ gH}_2/\text{L}$  and  $2\text{-}25\text{ wt. \% H}_2$ , respectively), their high

dehydrogenation enthalpies, leading to high operating temperatures obstruct their practical uses in PEMFCs.

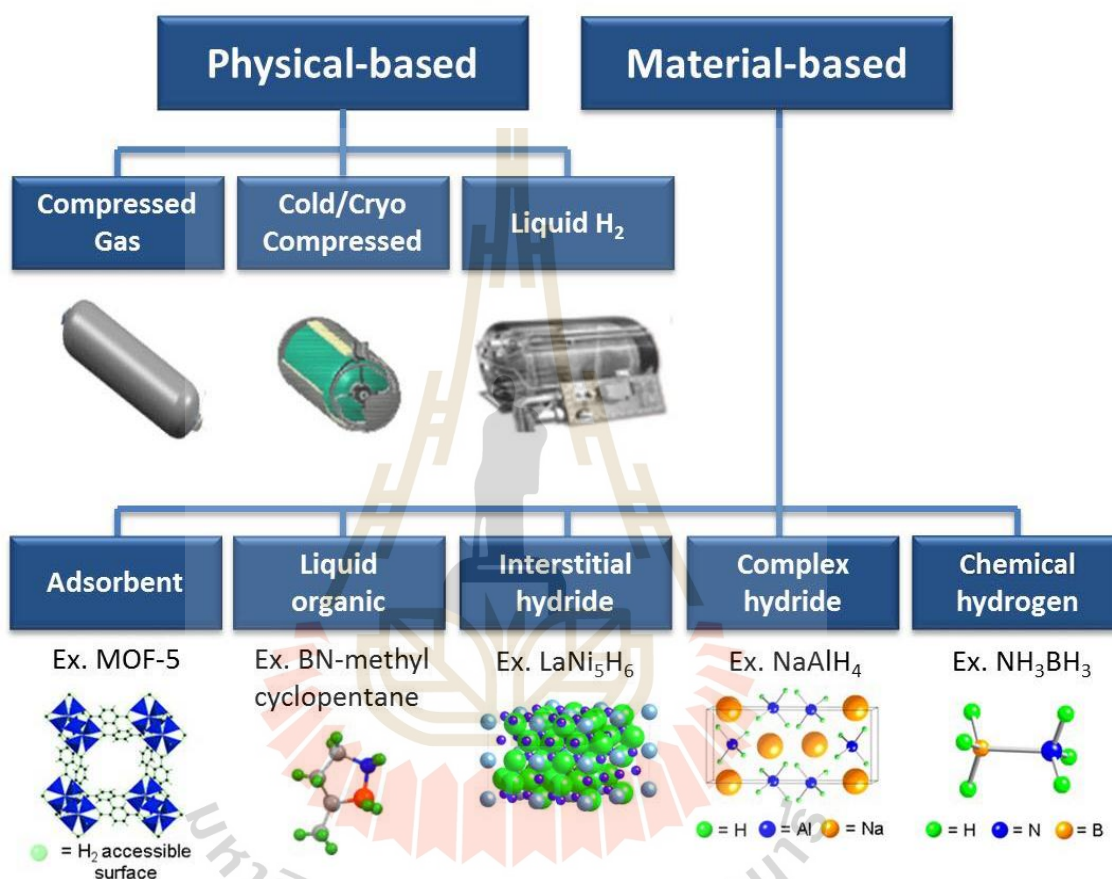


**Figure 1.2** Physical- and material-based hydrogen storages. (U. S. Department of Energy, 2017)

Hydrogen physisorption depending on the interaction between hydrogen molecules and adsorbents through Van der Waals force is relatively easy to handle and completely reversible due to low binding energy (4-10 kJ/mol) and fast adsorption kinetic (Abdalla et al., 2018 and Larminie et al., 2003). However, reasonable

hydrogen adsorption capacity can be achieved only at lower temperatures (77 K) due to low binding energy between hydrogen and adsorbents. This binding energy can be raised by three methods, including (i) the increase of physisorption (ii) Kubus binding, and (iii) spillover effect (Ströbel et al., 2006). The increase of physisorption is done by optimizing the interlayer distance between graphene layers for the hydrogen atoms and addition of additives to build a strong interaction with hydrogen (Elyassi et al. 2017). For Kubus binding of organometallic complexes, transition metals interact with hydrogen molecules via electron transfer from d-orbital of the transition metal to 1s orbital of hydrogen (Langmi et al., 2014). Spillover effect relies on transition metals depositing on porous adsorbents, acting as catalytic active centers for the dissociation of hydrogen molecules. From Figure 1.3, hydrogen spill has the following steps: The first  $H_2$  molecules undergo dissociative on the metal surfaces. After the first layer of dissociative hydrogen adsorption onto metal particles was formed. The second hydrogen molecules can be physisorbed and changed partially to polar molecules indicating physical bonds of hydrogen molecules on the metal surfaces. The third hydrogen molecules physisorbed on the metal surfaces can spill and diffuse freely to the surface [Park et al., 2008].

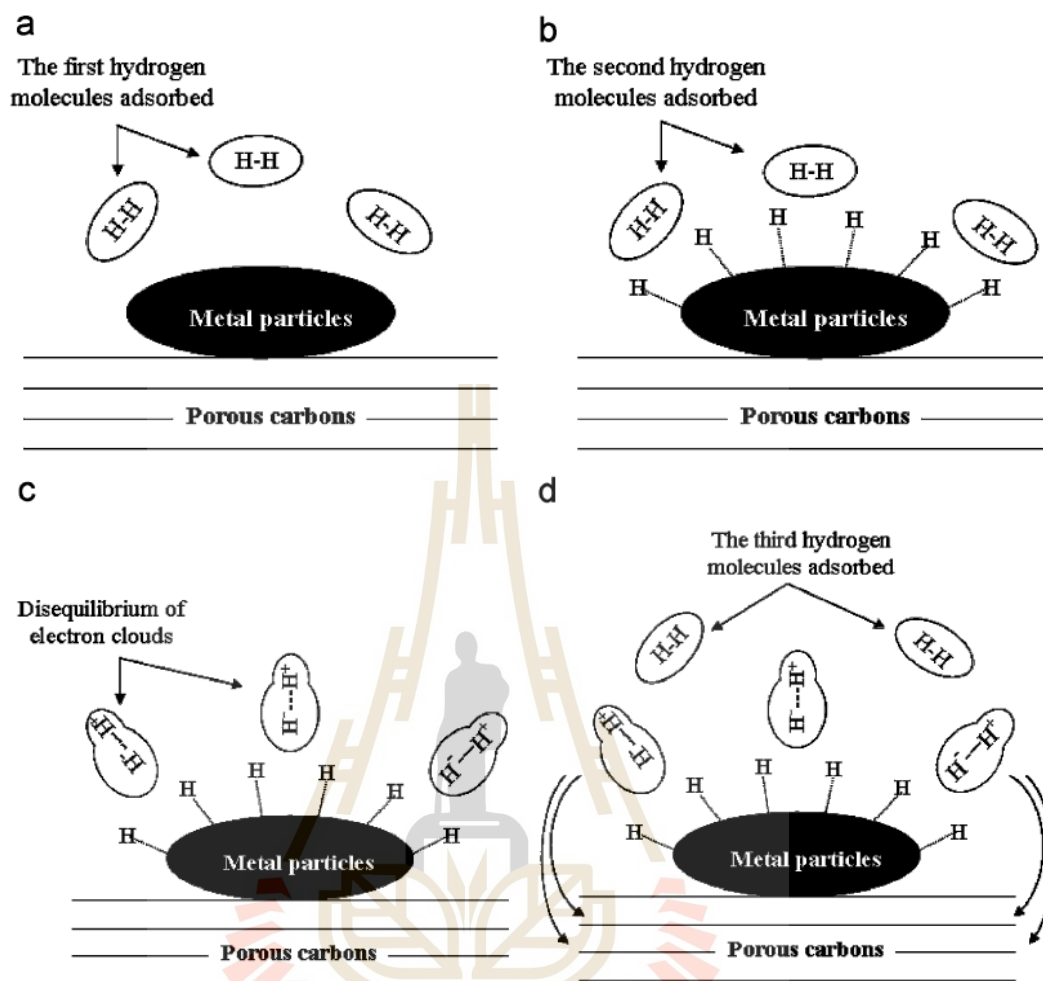
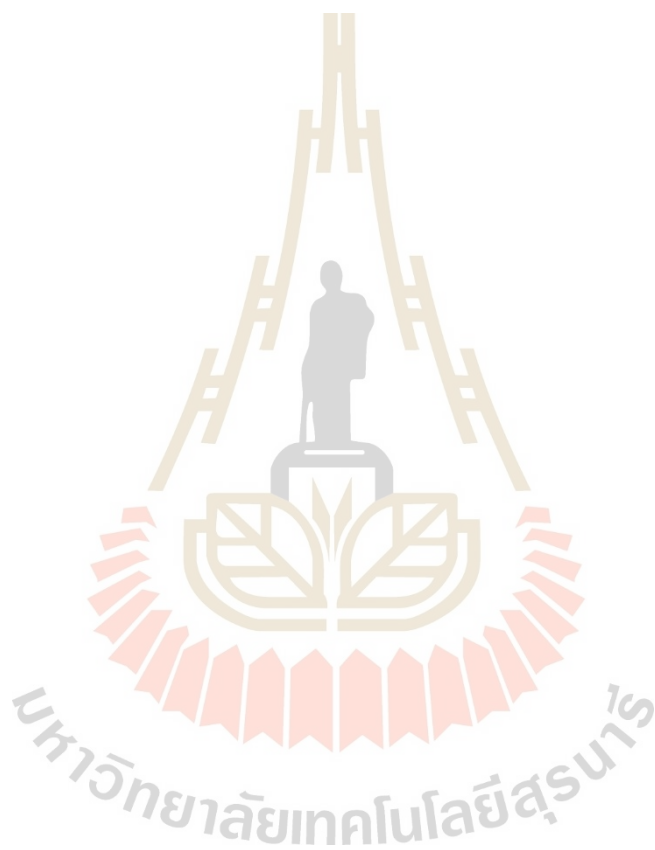


**Figure 1.3** Hydrogen spillover mechanism. (Park et al., 2008)

In this work, we aim to develop carbon-based adsorbent (activated carbon nanofibers) doped with Ni nanoparticles for hydrogen adsorption at ambient temperature (25 °C). Polyacrylonitrile (PAN) and polyvinylpyrrolidone (PVP) polymer are used as precursor solution for electrospinning. Decomposition of PVP during carbonization generates considerable porosity in PAN-PVP-based carbon nanofibers. N-rich formula of PAN benefits the dispersion of Ni nanoparticles onto

carbon surface and hydrogen adsorption. Hydrogen adsorption mechanisms into Ni-doped activated carbon nanofibers are investigated.



## CHAPTER II

### LITERATURE REVIEWS

Porous carbon materials (e.g., graphene, single-walled carbon nanotubes (SWCNTs), multi-walled carbon nanotubes (MWCNTs), activated carbon (AC), and carbon nanofibers (CNFs) (Figure 2.1)) have been studied for hydrogen adsorption because of their low density, high stability, high surface area and porosity, good thermal and chemical stability, variety of precursors, and low cost (Kim et al., 2007 and Xia et al., 2014). However, they can store hydrogen with reasonable capacity only under cryogenic temperature due to low binding energy (4-5 kJ/mol), while suitable energy for operating under ambient temperature is 15-25 kJ/mol (Li et al., 2006).



**Figure 2.1** Porous carbon materials.

Hydrogen adsorption onto porous carbons materials can be improved by increasing specific surface area via several physical and chemical treatments. For example, AC treated with HF showed specific surface area up to 884 m<sup>2</sup>/g and adsorbed 0.65 wt.% H<sub>2</sub> at 298 K under 35 bar H<sub>2</sub> (Jiménez et al., 2010). Another AC obtained from carbonization and chemical activation of coconut shell with high specific surface area of 2800 m<sup>2</sup>/g revealed adsorption capacity of 0.85 wt.% H<sub>2</sub> at 298 K under 100 bar H<sub>2</sub> (Jin et al., 2007). Ji et al. (Ji et al., 2007) found that hydrogen adsorption capacity of activated carbon nanofibers (ACNFs) (0.5-1.0 wt.%) increased with surface area, while unactivated CNFs could not adsorb hydrogen under the same condition (303 K under 30 bar H<sub>2</sub>). Furthermore, the adsorption performances of porous carbons can be enhanced by introduction of heteroatoms (e.g., B and N) into the carbon rings. This can induce electron deficiency and increase the polarity of carbon framework, strengthening H<sub>2</sub> interaction with the adsorbent (Kuchta et al., 2010). By incorporation of N into graphene (N-doped graphene), high specific surface area and microporous area increased from 78 m<sup>2</sup>/g and 10.8 m<sup>2</sup>/g, respectively, to 580 m<sup>2</sup>/g and 396 m<sup>2</sup>/g, respectively. N-doped graphene adsorbed ~1.5 wt. % H<sub>2</sub> at room temperature under 90 bar H<sub>2</sub>, while graphene oxide could perform only ~0.21 wt. % H<sub>2</sub> (Arjunan et al., 2017). Carbon xerogels (CX) doped with N (Figure 2.2) with high specific surface area and microporous area of 1602 m<sup>2</sup>/g and 1384 m<sup>2</sup>/g, respectively, adsorbed 0.28 wt. % H<sub>2</sub> at 35 °C under 50 bar H<sub>2</sub> (Kyung et al., 2009). Introduction of N into CX led to the enhancement of micropores, active sites for hydrogen dissociation.

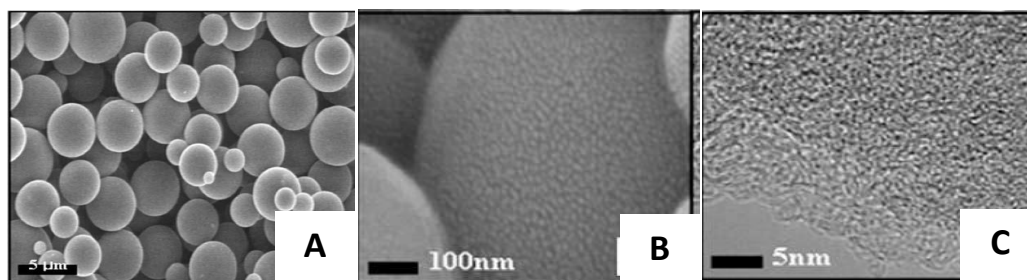


**Figure 2.2** FE-SEM images with different magnifications of N-doped CX.

(Kyung et al., 2009)

B-substituted carbon nanotubes (B-CNT) prepared by template assisted method adsorbed 2.0 wt. %  $H_2$  ( $T=300$  K and  $p(H_2) = 80$  bar) (Sankaran et al., 2007). Furthermore, B-N co-doped CNTs synthesized by chemical vapor deposition showed hydrogen adsorption capacity of 0.35 wt. %  $H_2$  ( $T= 303$  K and  $p(H_2) = 16$  bar) [Sawant et al., 2020]. In the literatures, several precursors containing nitrogen and carbon in their chemical structure have been proposed for synthesizing N-doped carbon materials e.g., acetonitrile (Reddy et al., 2010), melamine (Liu et al., 2014) and polyacrylonitrile and polyrhodanine (Quan et al., 2015 and Roberts et al., 2014).

Another approach to increase hydrogen adsorption capacity at room temperature is spillover by loading metal nanoparticles (e.g. Pt, Pd, Ru, Co, and Ni) into porous adsorbents. Pt doped into several porous adsorbents, for example, hydrogen induced exfoliated graphene (HEG), activated carbon, and MWCNTs (Divya et al., 2014, Seemita et al., 2015, Yang et al., 2009, and Zhao et al., 2012), adsorbed hydrogen in the range of 0.29-1.4 wt. %  $H_2$  ( $T = 298$  K,  $p(H_2) = 30$ -100 bar). Moreover, Co/Ru and Pd/Pt Co-doping into porous carbons showed hydrogen capacities of 0.45-1.65 wt. %  $H_2$  at 298 K under 50-75 bar  $H_2$  (Chen et al., 2014, Geng et al., 2014, and

Huang et al., 2013). Among various transition metals, Ni nanoparticles is particularly promising due to its performance, abundance, and low cost. CNTs with capillary and intertubular structure loaded with 2-20 wt. % Ni showed slight reduction of the specific surface area and total pore volume with increased Ni content due to pore blocking (Figure 2.3). Hydrogen adsorption capacity at 298 K under 100 bar H<sub>2</sub> of CNTs increased from 0.36 to 0.4-0.87 wt.% H<sub>2</sub> after doping with Ni (Han et al., 2017).

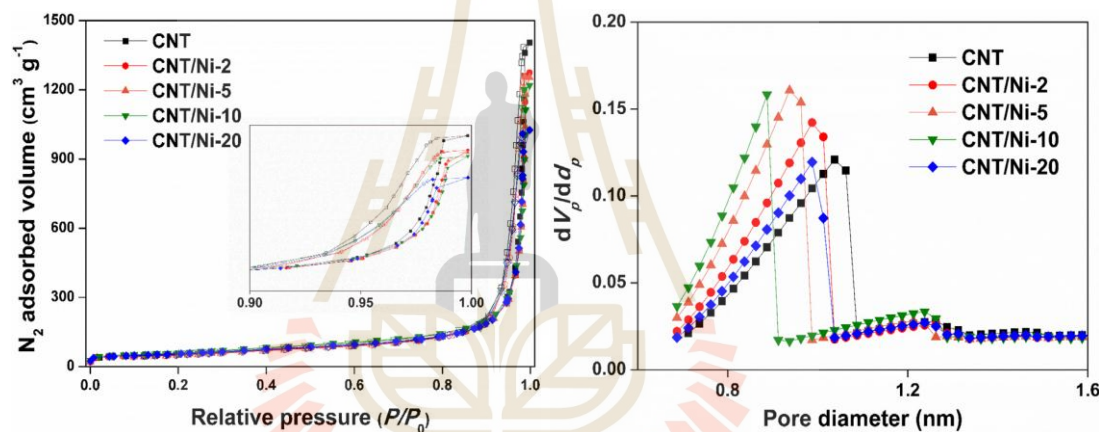


**Figure 2.3** N<sub>2</sub> adsorption-desorption isotherms of the CNTs and Ni-doped CNTs.

(Han et al., 2017)

Furthermore, Kuan-Yu et al. (Kuan et al., 2010) studied the effects of Ni particle sizes in Ni-doped MWCNTs (2 to 15 nm) on hydrogen adsorption. The sample loaded with Ni nanoparticles (5 nm) revealed the best adsorption of 1.02 wt.% H<sub>2</sub> at 25 ° C under 69 bar H<sub>2</sub> due to the good dispersion of Ni nanoparticles. Another Ni-doped MWCNT (10 wt. % Ni) adsorbed 0.114-0.298 wt. % H<sub>2</sub> at 298 K under 4-20 bar H<sub>2</sub> due to

physisorption and hydrogen spillover (Kaskun et al., 2018). It was found that multi-layer structure of MWCNT favors uniform distribution of metal nanoparticles and provides more active sites for hydrogen adsorption.

Activated carbon (AC) showed the maintained specific surface area and total pore volume after doping with Ni (1012-1013.4 m<sup>2</sup>/g and 0.40-0.42 cm<sup>3</sup>/g, respectively), indicating good dispersion of Ni nanoparticles. Ni-doped AC adsorbed 0.44 wt. % at 298 K under 10 bar H<sub>2</sub> (Nazlina et al., 2019). Furthermore, carbon nanofibers (CNFs) synthesized from various synthetic carbon precursors (i.e. polymer precursor, graphite, and benzene (Ashish et al., 2017, Byung et al., 2008, and Reddy et al., 2010)) and via different synthesis routes (i.e. electrospinning, chemical vapor deposition, and electrostatic assembly method (Ashish et al., 2017 and Byung et al., 2008)) have been proposed for storing hydrogen. Activated carbon nanofibers (ACNFs) loaded with Ni nanoparticles (ACNFs-Ni) showed that microporous volume was not substantially changed after of Ni doping (Lee et al., 2007). Small pores could encourage the interaction between hydrogen molecules and pore walls of adsorbents, enhancing hydrogen adsorption capacity. From Figure 2.4, ACNFs-Ni adsorbed 1.7 wt.% H<sub>2</sub> at 303 K under 100 bar H<sub>2</sub>, while ACNFs adsorbed only 1.0-1.2 wt.% because of spillover effect of Ni nanoparticles and high specific surface area.

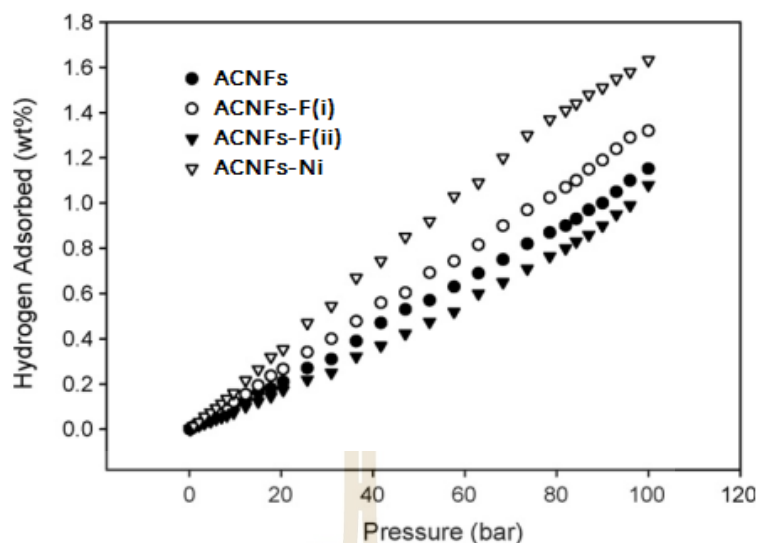


**Figure 2.4** Hydrogen adsorption isotherms of the ACNFs and ACNFs-Ni at 303 K up to 100 bar H<sub>2</sub>. (Lee et al., 2007)

Porous carbon nanofiber (PCNF) doped with 0.3-8.2 wt. % Ni plates showed the enhanced hydrogen adsorption with Ni loading content (Figure 2.5(A)) (Byung et al., 2008). Although PCNF has the highest specific surface of 1950 m<sup>2</sup>/g, only 0.2 wt. % H<sub>2</sub> could be adsorbed due to low adsorption energy on carbon supports. For PCNF-Ni, up to 2.2 wt.% H<sub>2</sub> at 298 K under 100 bar H<sub>2</sub> and fully reversible due to spillover effect and good dispersion of Ni were obtained. Moreover, activated carbon fiber (ACF) and graphitic carbon microfiber (CNF) synthesized from phenolic resin and doped with Ni nanoparticles showed the highest adsorption capacity of 0.75 wt. % H<sub>2</sub> (T=298 K under 50 bar H<sub>2</sub>) due to graphitic texture and spillover effect (Ashish et al., 2017). Although microporous structure of CNF benefited hydrogen adsorption, it was easily blocked by the addition of metal particles, resulting in poor hydrogen adsorption.

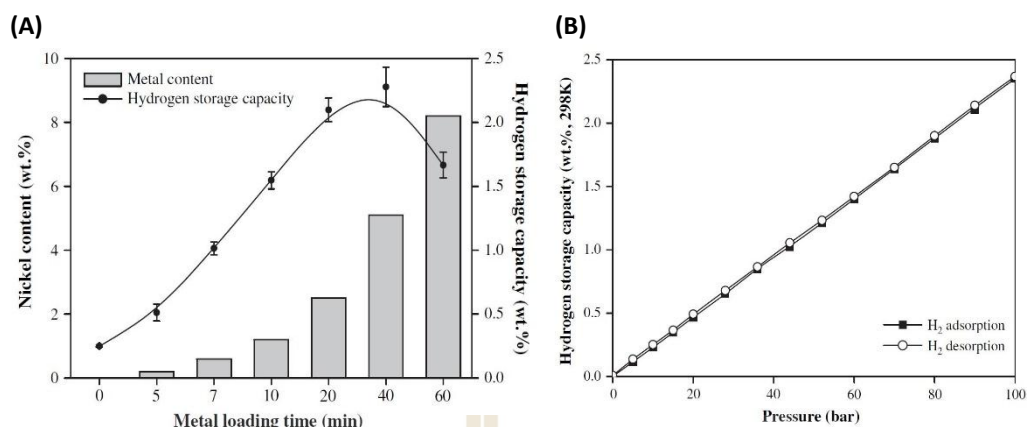


**Figure 2.5** The relationship between Ni loading content and hydrogen adsorption capacity of PCNF(A) and PCNF-Ni at 298 K(B). (Byung et al., 2008)

In this work, we would like to propose Ni-doped activated carbon nanofibers (ACNF) with high surface area and porosity. ACNF is prepared by chemical activation of electrospun polyacrylonitrile (PAN)-polyvinylpyrrolidone (PVP) nanofibers. It is expected that N-rich formula of PAN will enhance polarity of carbon favoring hydrogen adsorption and improve the dispersion of Ni nanoparticles onto ACNF surface. Moreover, ACNF with mixed meso- and microporous structures, leading to interconnected framework benefits mass transport channels for hydrogen diffusion. Ni nanoparticles doped into ACNF enhance hydrogen adsorption capacity via dissociative adsorption at room temperature.

## CHAPTER III

### EXPERIMENTS

#### 3.1 Materials

1. Polyacrylonitrile (PAN),  $M_w = 85,000$  g/mol HAIHANG INDUSTRY CO., LTD., China
2. Polyvinylpyrrolidone (PVP),  $M_w = 1,300,000$  g/mol, Aldrich
3. Nickel(II) nitrate hexahydrate ( $\text{Ni}(\text{NO}_3)_2 \cdot 6\text{H}_2\text{O}$ ),  $M_w=290.80$  g/mol, LOBA CHEMIE, AR grade, Purity 99 %
4. N,N-Dimethylformamide (DMF),  $d=0.944$  g/ml, Sigma-Aldrich

#### 3.2 Sample preparation

##### 3.2.1 Preparation of activated carbon nanofibers

Polyacrylonitrile (PAN, Haihang Industry Co., Ltd., China) precursor solution for electrospinning (18% w/w) was prepared by dissolving in N, N-dimethylformamide (DMF, Sigma-Aldrich) and stirring at room temperature for 12 h. For PAN-Polyvinylpyrrolidone (PVP) precursor solution, 8 wt. % PAN and 10 wt. % PVP (Aldrich) in DMF were prepared

by stirring at room temperature for 12 h. Both precursor solutions were loaded into a plastic bath and electrospinning was carried out at room temperature by using a Nanospider™ needle-less electrospinning technique (an Elmarco NS LAB 500, USA). Electrospinning was carried out at room temperature using a tip-to-collector distance and a high voltage of 21 cm and 40-45 kV, respectively. The obtained PAN and PAN-PVP based nanofibers were dried at 70 °C to remove the residual solvent and stabilized in air at 280 °C for 3 h (rate 1.5 °C/min). The stabilized nanofibers were carbonized at 1000 °C under N<sub>2</sub> atmosphere for 1 h to obtain carbon nanofibers. Chemical activation was done by immersing carbon nanofibers into concentrated KOH solution (30% w/v) at 80 °C for 2 h and drying at room temperature for 24 h. KOH-treated carbon nanofibers were activated by heating to 800 °C (heating rate 5 °C/min) under N<sub>2</sub> atmosphere, dwelling at 800 °C for 15 min, and cooling to room temperature to obtain activated carbon nanofibers, denoted as ACNF and ACNF-PVP. To neutralize residual KOH, ACNF and ACNF-PVP were immersed in 0.5 M hydrochloric acid (HCl) at room temperature for 30 min, filtered, and washed with distilled water until neutral pH was reached. The obtained activated carbon nanofibers were dried at 120 °C for 24 h and at 500 °C under vacuum for 5 h.

### 3.2.2 Preparation of Ni-doped ACNF-PVP

ACNF-PVP was loaded with Ni nanoparticles (5, 10, and 20 wt. %) by wet impregnation method using nickel (II) nitrate hexahydrate (Ni(NO<sub>3</sub>)<sub>2</sub> · 6H<sub>2</sub>O, LOBA CHEMIE) as Ni source. ACNF-PVP (~10 g) were dispersed in 10.00 mL of 24.80, 49.55, and 99.10 % w/v Ni(NO<sub>3</sub>)<sub>2</sub>·6H<sub>2</sub>O in acetone by sonication at room temperature for 1 h to

prepare 5, 10, and 20 wt. % Ni-doped ACNF-PVP, respectively. The sample was dried at 100 °C under N<sub>2</sub> atmosphere for 1 h. The sample was reduced by heating the sample to 350 °C under 5 % H<sub>2</sub> in Ar atmosphere for 5 h. Ni-doped ACNF-PVP samples were labeled according to Ni-loading contents, i.e., 5Ni-ACNF-PVP, 10Ni-ACNF-PVP, and 20Ni-ACNF-PVP for the samples with 5, 10, and 20 wt. % Ni, respectively.

### 3.3 Characterizations

Morphology and elemental distribution of all samples were characterized by scanning electron microscopy (SEM) and elemental mapping technique, respectively. All samples were deposited on the sample holders by using silver glue in n-butyl acetate. Evaporation of n-butyl acetate was carried out at room temperature for 1-2 h. Morphology of ACNF was studied by using an Auriga from Zeiss, Germany. For Ni-doped ACNF-PVP, morphology and elemental distribution (Nickel (Ni), carbon (C), and oxygen (O)) were characterized by an apparatus from EDAX Inc. Texture parameters based on specific surface area, pore size, and pore volume of all samples were determined by N<sub>2</sub> adsorption-desorption technique using a Micromeritics 3Flex physisorption at 77 K. Prior to the measurements, known amounts of all samples were degassed at 250 °C under vacuum for 16 h. All samples were studied with a full adsorption and desorption isotherm ( $p/p_0=0-1$ ) at liquid nitrogen temperature with nitrogen gas as an adsorbent. Ni loading contents were characterized by ICP-OES using a Perkin Elmer Optima 7300DV with ASTM D6357 test method. The sample was digestion in microwave oven. The obtained sample (~0.20 g) was mixed with 20 mL aqua regia and concentrated HCl. The mixture was heated to 130-150

°C and kept at isothermal condition until dryness. The sample was dissolved in 1 mL concentrated HNO<sub>3</sub> and 20 mL deionized water, heated to 90-100 °C, and cooled to room temperature. The sample solution diluted with deionized water was used for the measurements and Ni (NO<sub>3</sub>)<sub>2</sub> solutions (1-20 ppm) were used as the standard solutions.

Raman spectra of all samples were obtained by using a NT-MDT, NTEGRA Spectra equipped with an Olympus microscope. The laser spot was focused by an objective lens of 100x. The experiment was carried out at an excitation wavelength of 532 nm and Raman spectra were collected with an exposure time of 10 s for 12 cycles. Raman active peak of silicon at 521 cm<sup>-1</sup> was used for calibration. X-ray diffraction (XRD) of all samples were performed by using a Bruker D2 PHASER with a Cu K<sub>α</sub> radiation ( $\lambda = 0.15406$  nm). The diffraction patterns were collected in the 2 $\theta$  range of 10-100° and the scanning step of 0.02°/s. Fourier transform infrared (FTIR) spectra were collected using a Bruker, IR spectrometer (Tensor 27). The sample was ground with anhydrous KBr (1:10 weight ratio of sample:anhydrous KBr) and pressed under 10 tons for 2 min to obtain KBr pellet. The sample was assembled in the FTIR machine on the direction of infrared. The spectrum was recorded in the wavenumber range of 4000-400 cm<sup>-1</sup> with 64 scans for both samples and background.

Hydrogen ad/desorption experiments were carried out using a test station automatically controlled by the software developed in a LabVIEW® environment (Figure 3.1). The powder sample (0.5-1.0 g) was packed in a high-pressure sample cell (316SS, Swagelok) under N<sub>2</sub> atmosphere in the glove box, and transferred to the test station.

Hydrogen pressure in system was adjusted by the direct-acting plunger solenoid valves (Type 0255, Bürkert). Hydrogen content released during desorption was measured by a mass flow controller (MFC, a Bronkhorst EL-FLOW High pressure model F-221M-RAD-22-V) with operating flow rate of 0-0.1 standard L/min (SLM) at standard temperature ( $T_s$ ) and pressure ( $P_s$ ) of 294.95 K and 1.0167 bar, respectively. Pressure transducers with operating pressures of 0-100 bar (Kistler type 4260A) and K-type thermocouples (-250 to 1300 °C, SL heater) were used to measure pressure and temperature, respectively. Temperature pressure, and mass flow rate signals were transferred to the computer by using the module data loggers (NI USB-6009, National Instruments and AI210, Wisco). Prior to the experiments, void volumes of the sample and reference cells after filling with the powder sample and dried sand, respectively, were measured and equally adjusted. Hydrogen adsorption was carried out by degassing at 300 °C under vacuum for 3 h and cool down to 25 °C.

Hydrogen adsorption was done at isothermal condition ( $T=25$  °C) under 20-100 bar  $H_2$  for 5 h. When adsorption completed, hydrogen pressures in the sample and reference cells were adjusted to equal. Hydrogen desorption was carried out by heating both sample and reference cells to 50 °C (5 °C/min) and hydrogen release from each cell were detected by MFC. Hydrogen volume (SL) was calculated by integrating the peak area of the hydrogen flow rate (SLM) versus time (min) plot. Hydrogen storage capacity was calculated from the difference of hydrogen amounts released from the sample and reference cells by using the following equations.

$$V_{\text{STP}} = \frac{P_s V_s T_{\text{STP}}}{T_s P_{\text{STP}}} \quad (1)$$

$$n_{\text{H}_2} = \frac{V_{\text{STP}}}{22.4 \frac{\text{L}}{\text{mol}}} \quad (2)$$

$$\text{H}_2 \text{ capacity (wt. \%)} = \frac{n_{\text{H}_2} \times 2.016 \frac{\text{g}}{\text{mol}}}{\text{sample weight}} \times 100 \quad (3)$$

where  $V_{\text{STP}}$  (L) and  $V_s$  (SL) are volumes of hydrogen gas at standard temperature and pressure condition (STP,  $T_{\text{STP}} = 273.15$  K and  $P_{\text{STP}} = 1.0133$  bar) and at standard condition of MFC, respectively.  $n_{\text{H}_2}$  (mol) is hydrogen moles and standard molar volume is 22.4 L/mol.

X-ray photoelectron spectroscopy (XPS) of samples was carried out at the SUT-NANOTEC-SLRI, BL 5.2: SUT-NANOTEC-SLRI, Synchrotron Light Research Institute (Public Organization), Thailand. The measurement was done using a PHI5000 Versa Probe II (ULVAC-PHI Inc., Japan) with Al Ka (1.486 keV) radiation as an excitation source. The samples were deposited in high vacuum chamber ( $1 \times 10^{-8}$  mbar) for 2 h. Each element was investigated at an energy step and a part energy of 0.05 eV and 46.95 eV, respectively. The number of scans for C 1s and Ni 2p XPS spectra were 3 and 10 scans, respectively. The binding energy was calibrated with respect to the C 1s peak (284.8 eV). All spectra were fitted to mixed Gaussian-Lorentzian by using a Multipak software. X-ray absorption spectroscopy (XAS) was performed at the BL2.2: TRXAS, Synchrotron Light Research Institute (SLRI), Thailand. Ni K-edge XANES spectra were measured in transmission mode using a Si (220) bent crystal monochromator and analyzed by Athena program. The transmitted X-rays were detected simultaneously with a linear image NMOS sensor. The

powder sample of ACNF-PVP-5% Ni was prepared as a pellet of 5 mm diameter and placed into an in-situ cell for time-resolved XANES measurement. The temperature programmed reduction (TPR) experiment was conducted by heating the sample to 450 °C (5 °C/min) and dwelling at 450 °C for 60 min under H<sub>2</sub>/N<sub>2</sub> atmosphere with the flow rate of 24/76 ml/min. Hydrogen adsorption was done by cooling the compacted sample to 30 °C under the H<sub>2</sub> flow rate of 24 ml/min and keeping at isothermal condition for 30 min and desorption was continued by heating the sample to 200 °C (5 °C/min).

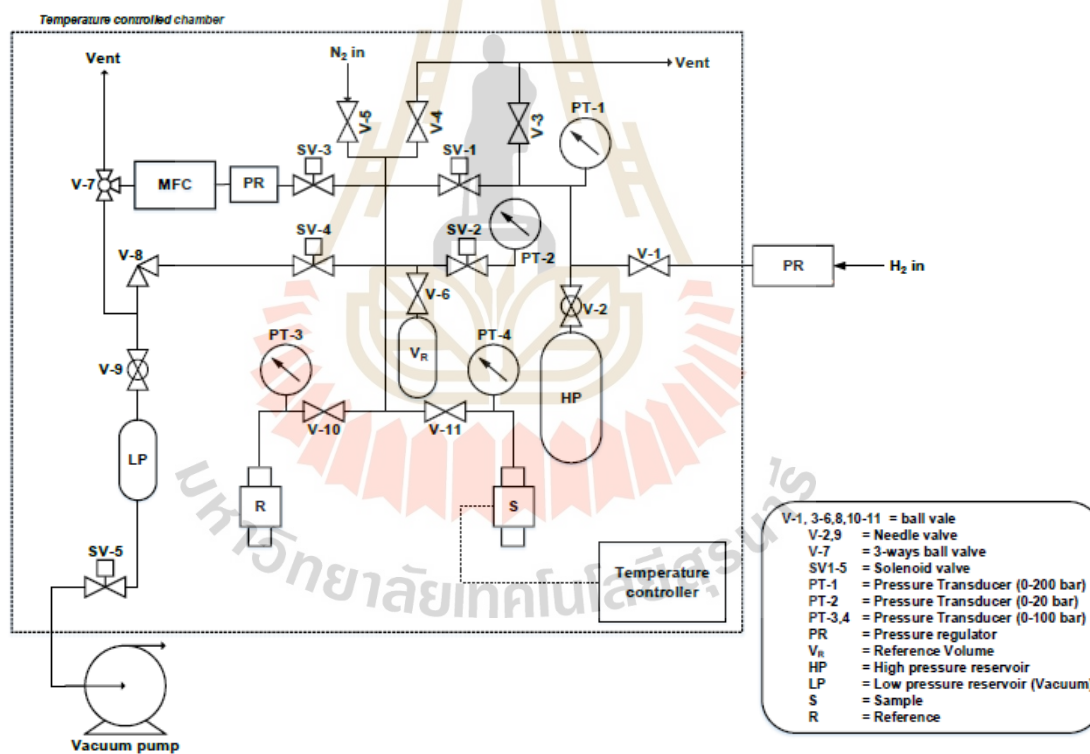


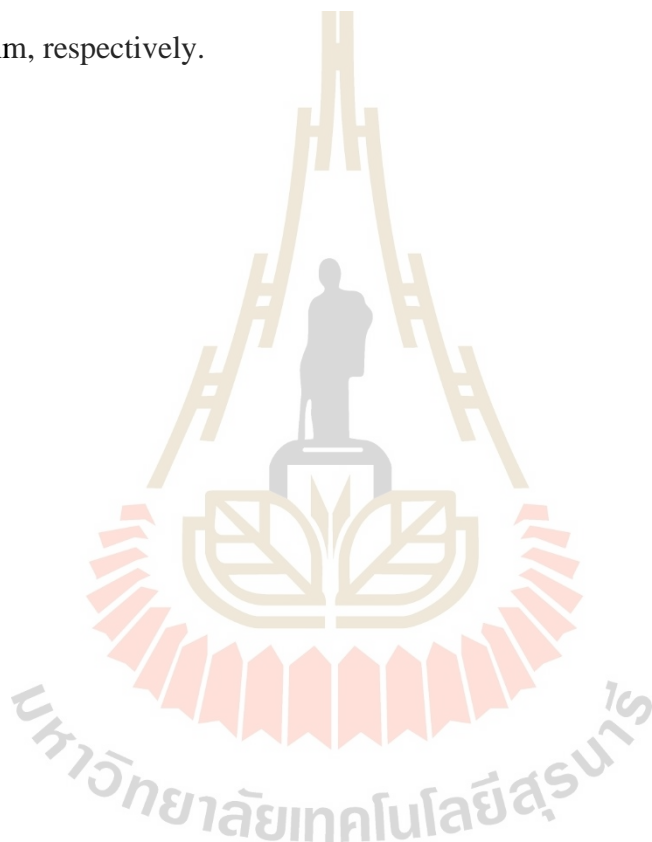
**Figure 3.1** Components of hydrogen ad/desorption test station.

### 3.4 Computations

Spin-polarized density functional theory (DFT) calculations were performed using the Vienna ab initio Simulation Package (VASP 5.3) (Kresse et al., 1996 and Perdew et al., 1996). The generalized gradient approximation with Perdew-Burke-Ernzerhof were used to treat the exchange-correlation functional of the interacting electrons (Kresse et al., 1999). The projector augmented wave method was employed to describe the nucleus and core electron potentials (Grimme et al., 2006). The weak van der Waals interactions were included using the Grimme's scheme of DFT-D3 corrections (Amaya-Roncancio et al., 2018 and Grimme et al., 2010). The plane wave cut-off energy was chosen to be 500 eV. The convergence criterion of total energy was set to  $10^{-6}$  eV, where the force convergence of ionic relaxation was set to 0.02 eV/Å. The icosahedral Ni<sub>13</sub> cluster (Lin et al., 2011 and Chaves et al., 2017) supported on pyrrolic graphene (Rangel et al., 2016) was used as a model with the Monkhorst-Pack sampling of 3×3×1 k-point mesh in the Brillouin zone (Monkhorst et al., 1976). The vacuum region of 15 Å was added to avoid the spurious interactions between periodic images. To find the most stable H<sub>2</sub>-adsorbed configurations, *ab initio* molecular dynamic (AIMD) simulations in an NVT ensemble was performed and setting temperature at 300 K using the Nosé-Hoover thermostat was applied (Nosé et al., 1984). The simulation was run for 1 ps with the time-step of 0.5 fs. Due to the large supercells, Brillouin zone integrations were sampled only at the  $\Gamma$ -point.

To directly compare the calculated atomic structure model with the experiments, Ni K-edge XANES spectra were simulated. The fully relaxed structure of the icosahedral Ni<sub>13</sub> cluster on pyrrolic graphene obtained from DFT calculation was used as an input

coordinates for FEFF8.2 codes (Rehr et al., 2009). The latter was employed to calculate Ni K-edge XANES spectrum based on the multiple-scattering expansion within the muffin-tin potentials. The Hedin-Lundqvist was used as the exchange-correlation potential with an imaginary part of 0.5 eV to simulate the experimental broadening (Hedin et al., 1971). The radii for self-consistent potential and full-multiple scattering calculations were set at 0.65 and 0.80 nm, respectively.



## CHAROTIION IV

### RESULTS AND DISCUSSION

#### 4.1 Morphology, textural parameters, and phase compositions

Texture parameter, porosity, and morphology of ACNF and ACNF-PVP are characterized by N<sub>2</sub> adsorption-desorption and SEM technique. From Figure 4.1, both ACNF and ACNF-PVP have fibrous structure and high porosity with average diameter of 200 nm. From table 4.1, specific surface area ( $S_{\text{BET}}$ ) and total pore volume ( $V_{\text{tot}}$ ) of ACNF are 676.4 m<sup>2</sup>/g and 0.37 m<sup>3</sup>/g, respectively. By using PVP as porous precursor,  $S_{\text{BET}}$  and  $V_{\text{tot}}$  increase to 763.4 m<sup>2</sup>/g and 0.41 m<sup>3</sup>/g, respectively, while pore diameter ( $D_{\text{max}}$ ) of 0.73 nm is maintained. The pore width (0.6-0.7 nm) was suitable for hydrogen physisorption because dynamic molecular hydrogen with diameter of 0.4059 nm could be trapped properly (Im et al, 2008). Decomposition of PVP well dispersed in PAN-PVP polymer nanofibers during carbonization and chemical activation enhances the proportion of micropores, increasing surface area and porosity in ACNF-PVP. Therefore, PAN-PVP composite is further used as precursor for preparation of activated carbon nanofibers.

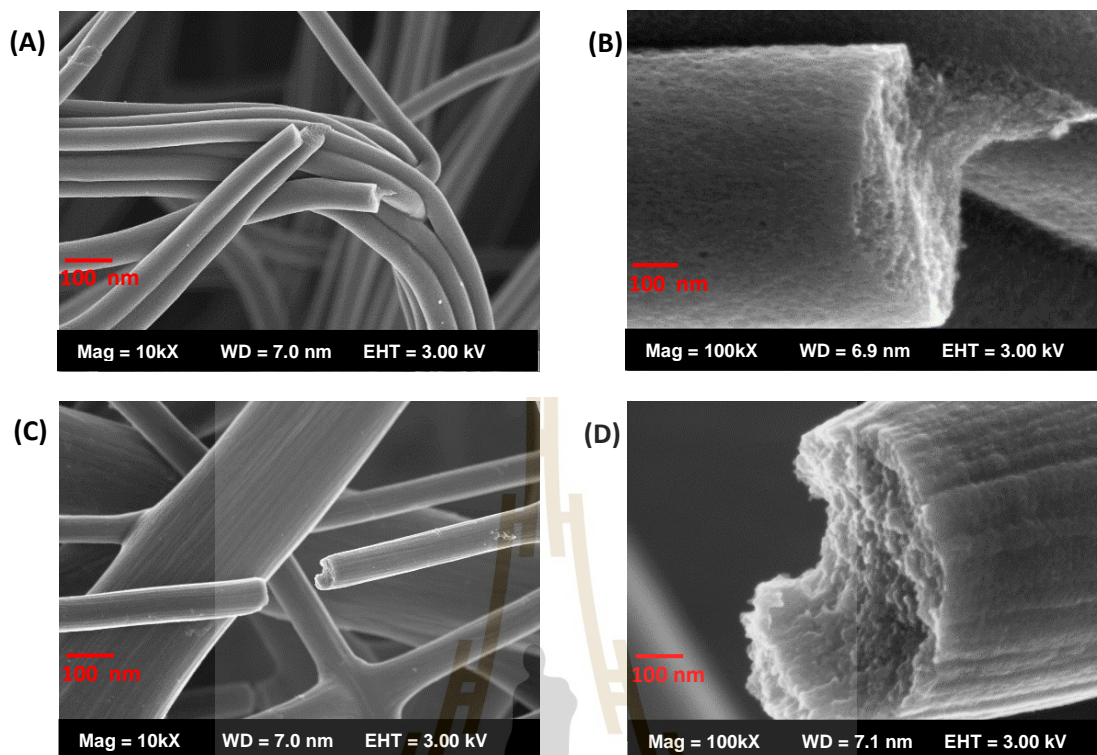
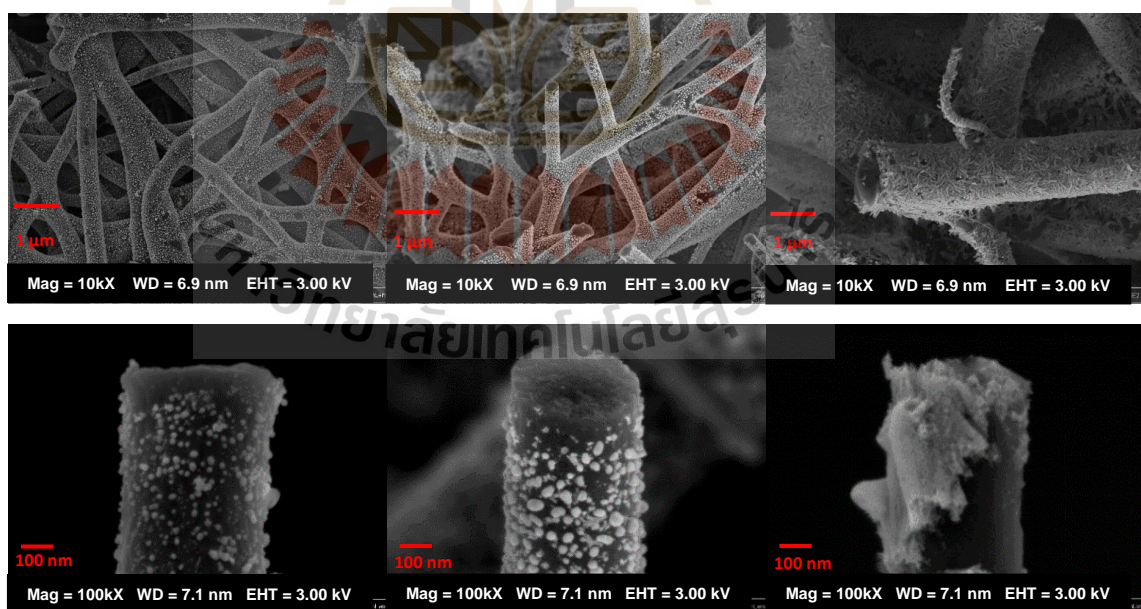


**Figure 4.1** SEM images of ACNF (A-B) and ACNF-PVP (C-D).

**Table 4.1.** Texture parameters of ACNF, ACNF-PVP, and 5Ni-ACNF/PVP.

| Samples      | $S_{BET}$<br>( $m^2g^{-1}$ ) | $V_{Total}$<br>( $cm^3g^{-1}$ ) | $V_{Meso}$<br>( $cm^3g^{-1}$ ) | $V_{Micro}$<br>( $cm^3g^{-1}$ ) | Aver pore<br>diameter(nm) |
|--------------|------------------------------|---------------------------------|--------------------------------|---------------------------------|---------------------------|
| ACNF         | 676.39                       | 0.366                           | 0.096                          | 0.237                           | 0.731                     |
| ACNF-PVP     | 763.40                       | 0.410                           | 0.100                          | 0.270                           | 0.734                     |
| 5Ni-ACNF-PVP | 675.96                       | 0.358                           | 0.080                          | 0.240                           | 0.713                     |

To study morphology and elemental dispersion of Ni-doped ACNF-PVP, all samples were characterized by scanning electron microscopy (SEM) and elemental mapping techniques. Fibrous structure of ACNF-PVP is maintained after Ni loading (5-20 wt. %) (Figure 4.2). 5Ni-ACNF-PVP (a-d) and 10Ni-ACNF-PVP (e-h) show good dispersion of Ni nanoparticles on the surface of ACNF-PVP with average particle sizes of 5-10 and 30-60 nm, respectively. However, particle agglomeration of Ni is found from 20Ni-ACNF-PVP (Figure 4.2 (i-l)) because of high Ni-loading content. To investigate the actual Ni loading contents of Ni-doped ACNF-PVP samples, ICP-OES technique is applied. Ni loading contents in 5Ni-ACNF-PVP, 10Ni-ACNF-PVP, and 20Ni-ACNF-PVP are 4.00, 8.25, and 16.50 wt. % Ni, respectively.



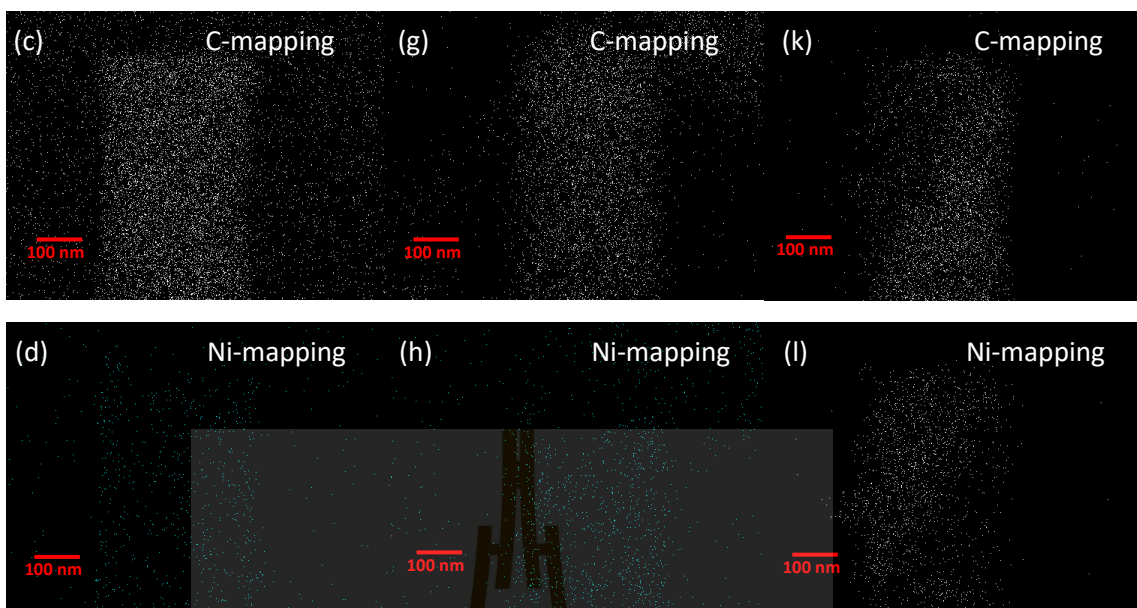


**Figure 4.2** SEM images of 5Ni-ACNF-PVP (a-d), 10Ni-ACNF-PVP (e-h) and 20Ni-ACNF-PVP (i-l).

Carbon structure of ACNF-PVP before and after Ni loading is characterized by Raman spectroscopy. From Figure 4.3, Raman spectra of all samples show two major vibrational peaks. The first peak (G-band) at  $1588\text{ cm}^{-1}$  indicates an in-plane stretching of  $\text{sp}^2$  carbon bonds in ideal graphitic lattice. The second peak (D band) at  $1358\text{ cm}^{-1}$  refers to the vibration of  $\text{sp}^3$  carbon from the disordered turbostratic structure or deficiencies in the carbon structure (Choi et al., 2013 and Bognitzki et al., 2001). Moreover, characteristic peaks of the disordered carbons at  $1185\text{ cm}^{-1}$  ( $\text{D}_1$  band) and  $1491\text{ cm}^{-1}$  ( $\text{D}_A$  band) are observed. These correspond to the defects from heterogeneous atoms (e.g., N and O) and amorphous carbon due to interstitial defects, respectively (Cuesta et al., 1994 and Jawhari et al., 1995). The microstructure disorder in carbon is evidenced by the integrated intensity ratio ( $I_{\text{D}}/I_{\text{G}}$ ) (Jawhari et al., 1995

and Zhou et al., 2014). The more the  $I_D/I_G$  ratio, the higher the microstructure disorder.  $I_D/I_G$  ratios of ACNF-PVP and 5Ni-ACNF-PVP are comparable (1.68-1.69). By increasing Ni loading content,  $I_D/I_G$  ratios of 10Ni-ACNF-PVP and 20Ni-ACNF-PVP increase to 1.73-1.88. This suggests that carbon microstructure of ACNF-PVP is maintained with Ni loading contents up to 5 wt. %, while higher Ni loading contents (10 and 20 wt. %) lead to disorder microstructure of ACNF-PVP.

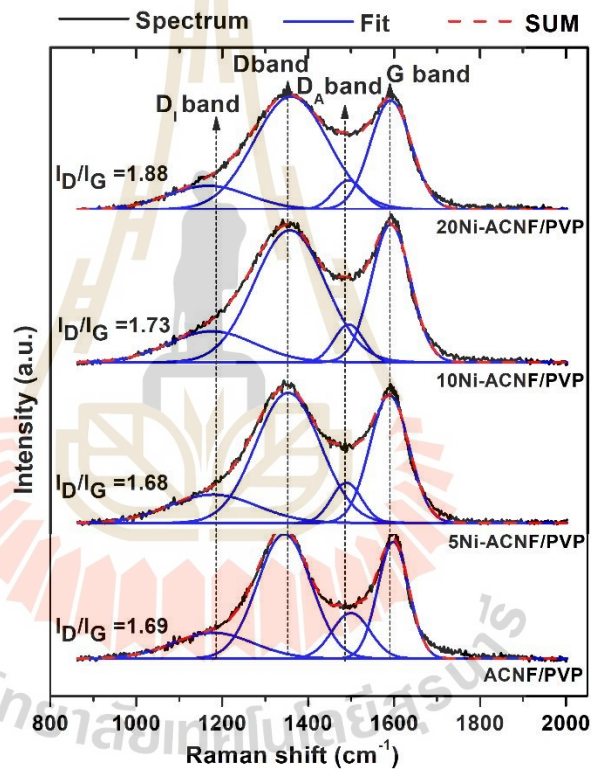


**Figure 4.3** Raman spectra of ACNF-PVP, 5Ni-ACNF-PVP, 10Ni-ACNF-PVP, and 20Ni-ACNF-PVP.

Furthermore, powder x-ray diffraction patterns (PXRD) of ACNF-PVP before and after doping with Ni were recorded to identify phase composition. From Figure 4.4, PXRD spectra of all samples show two broad peaks of carbon at  $2\theta \sim 25$  and  $43^\circ$ . In

addition, 5Ni-ACNF-PVP shows broader peaks of both metallic Ni and NiO than 10Ni-ACNF-PVP and 20Ni-ACNF-PVP, indicating amorphous state and/or nanoparticles Ni.

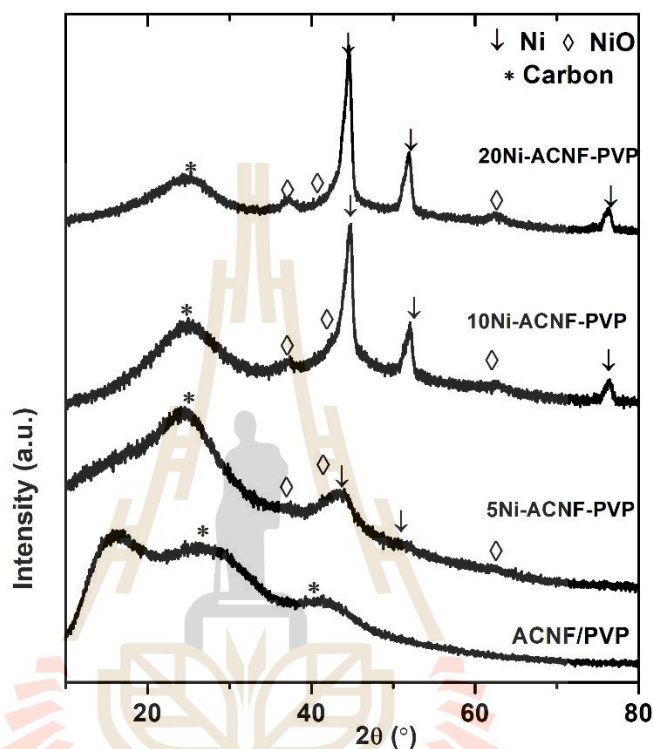


**Figure 4.4** PXD spectra of ACNF-PVP, 5Ni-ACNF-PVP, 10Ni-ACNF-PVP, and 20Ni-ACNF-PVP.

#### 4.2. Hydrogen adsorption performances and cycling stability

Hydrogen adsorption performance of all samples was performed at ambient temperature (25 °C). To compare the performance of all samples, hydrogen storage was carried out at ambient temperature under 50 bar H<sub>2</sub> for 5 h. From Figure 5, ACNF-PVP can adsorb up to 0.53 wt. % H<sub>2</sub>, while ACNF can adsorb 0.25 wt. % H<sub>2</sub> due to high specific surface area and porosity of ACNF-PVP. For Ni-doped ACNF-

PVP samples, hydrogen adsorption capacity of 5Ni-ACNF-PVP is up to 1.33 wt. % due to good distribution and small particle size of Ni nanoparticles. However, 10Ni-ACNF-PVP and 20Ni-ACNF-PVP can adsorb only 0.40-0.44 wt. %  $H_2$  due to Ni agglomeration.

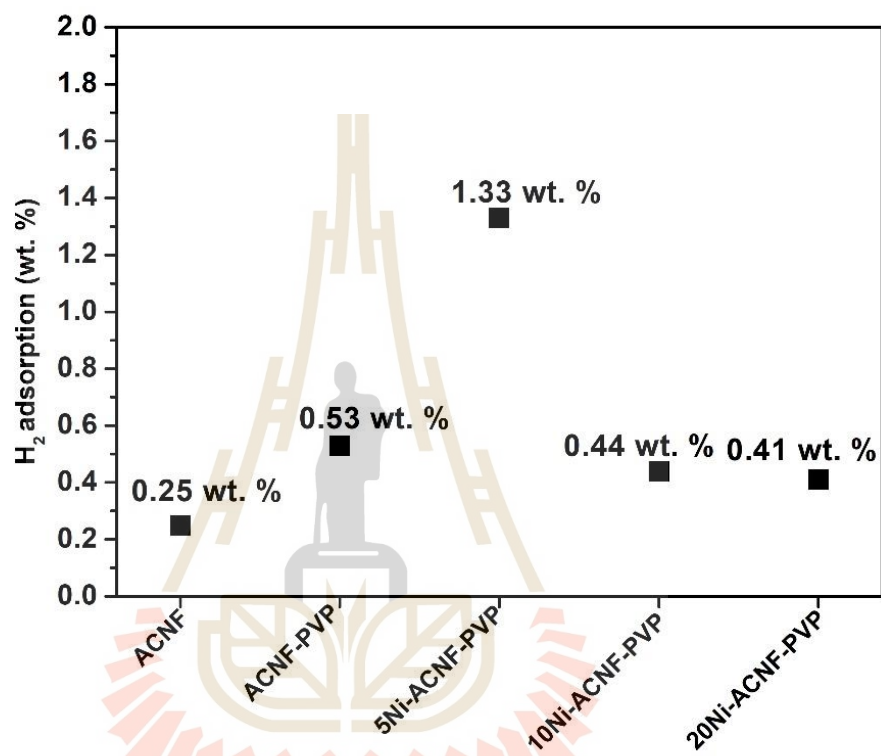


**Figure 4.5** Hydrogen adsorption of ACNF-PVP and Ni-doped ACNF-PVP (5-20 wt. %) at 25 °C under 50 bar  $H_2$  for 5 h.

Regarding the best performances of 5Ni-ACNF-PVP, it is further studied and compared with ACNF-PVP under hydrogen pressure of 20-100 bar at ambient temperature (25 °C). Hydrogen adsorption capacities of ACNF-PVP is 0.18-0.80 wt. %, while those of 5Ni-ACNF-PVP are up to 0.55-2.12 wt. %  $H_2$  (Figure 4.6 (A)). Furthermore, the cycling stability of 5Ni-ACNF-PVP upon 10 ad/desorption cycles

was studied under 50 bar  $H_2$ . Hydrogen storage capacities are preserved at average value of 1.17 wt. %  $H_2$  (Figure 4.6 (B)).

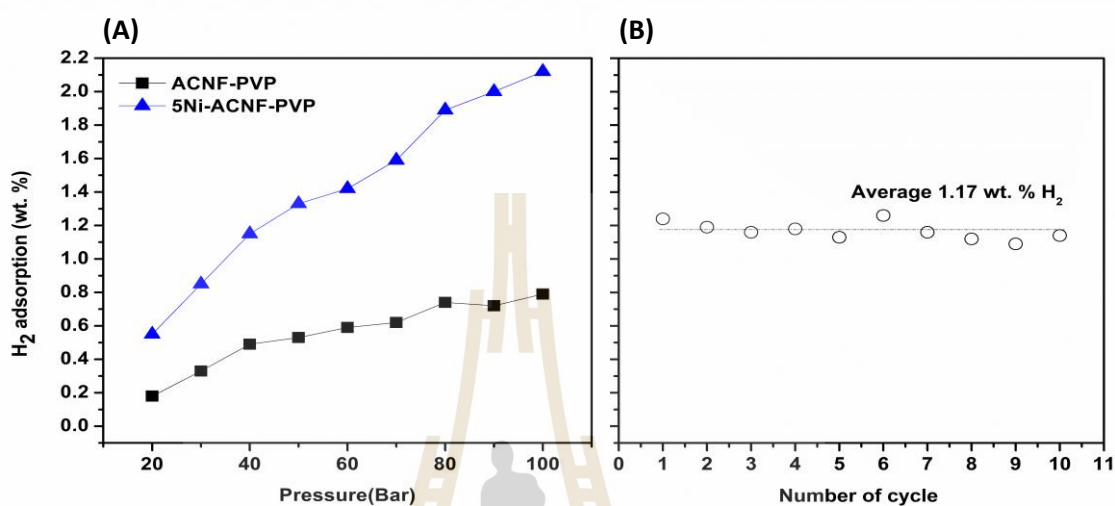


**Figure 4.6** Hydrogen adsorption at 25 °C under 20-100 bar  $H_2$  of ACNF-PVP and 5Ni-doped ACNF-PVP (A) and cycling stability upon 10 ad/desorption cycles of 5Ni-doped ACNF-PVP (B).

Furthermore, morphology and distribution of Ni nanoparticles of 5Ni-ACNF-PVP after cycling was investigated by SEM technique. From Figure 4.7, fibrous structure of ACNF-PVP is maintained with slight agglomeration of Ni nanoparticles. This implies good mechanical stability upon cycling of 5Ni-ACNF-PVP.

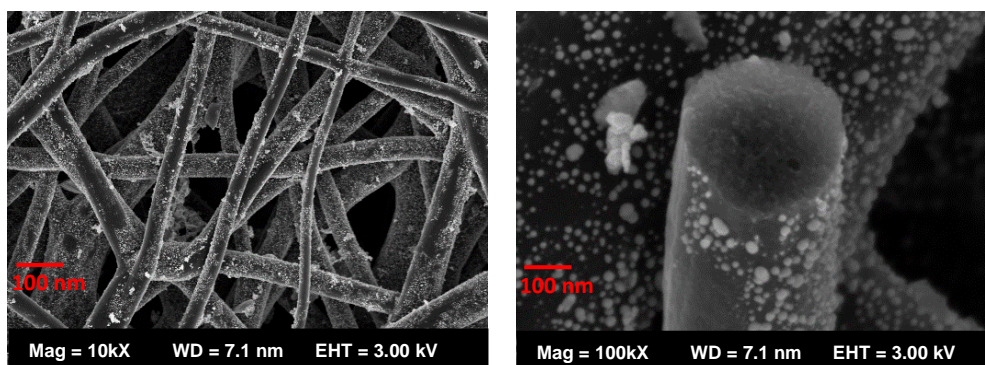


**Figure 4.7** SEM images of 5Ni-doped ACNF-PVP after the 10<sup>th</sup> desorption.

### 4.3. Textural parameters, Ni-carbon interaction, and hydrogen adsorption mechanisms

Texture parameters and chemical structure of ACNF-PVP before and after Ni loading (5 wt. %) as well as the interaction between ACNF-PVP and Ni nanoparticles are investigated by BET, FTIR, and XPS techniques. From Table 4.1,  $S_{\text{BET}}$  and  $V_{\text{total}}$  of 5Ni-ACNF-PVP (676.0 m<sup>2</sup>/g and 0.36 cm<sup>3</sup>/g, respectively) are lower than those of ACNF-PVP due to pore blocking of the dispersed Ni nanoparticles. ACNF-PVP and 5Ni-ACNF-PVP exhibit type I isotherm, suggesting material with pore distribution over the narrow range of micropores (Figure 4.8(A) (Lastoskie et al., 1993 and Zhao et al., 2019). Figure 4.8 (B) shows comparable pore size distributions of ACNF-PVP and 5Ni-ACNF-PVP, indicating the unchanged pore size after Ni loading.

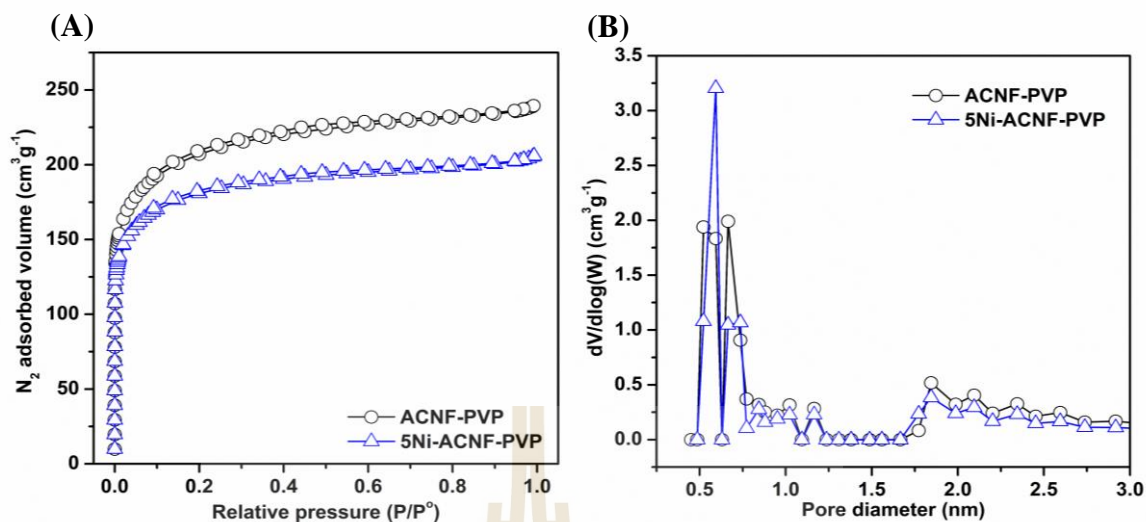


**Figure 4.8** N<sub>2</sub> adsorption isotherms(A) and pore size distribution(B) of ACNF-PVP and 5Ni-ACNF-PVP.

From Figure 4.9 (A), the chemical structure of ACNF-PVP before and after Ni loading (5 wt. %) is confirmed by FTIR technique. Both spectra of ACNF-PVP and 5Ni-ACNF-PVP display vibrational peaks of O-H and N-H stretching (3429 cm<sup>-1</sup>), C-H stretching (3006-2923 cm<sup>-1</sup>), sp<sup>2</sup> C=C stretching (1633 cm<sup>-1</sup>), C-NH stretching (1541 cm<sup>-1</sup>), C-H bending (1385 cm<sup>-1</sup>), and sp<sup>2</sup> C=N and sp<sup>2</sup> C-N stretching in triazine ring systems (strong peaks in the 1600-1200 cm<sup>-1</sup> region) (Liu et al., 2013, Eren et al., 2016, and Kim et al., 2015). These characteristic peaks correspond to the functional groups in chemical structure of PAN-based carbon nanofibers (Figure 4.9 (B)) (Ibupoto et al., 2018). The vibrational peaks of C=O stretching (1738-1716 cm<sup>-1</sup>), C-OH bending (1417 cm<sup>-1</sup>), and C-O stretching (1223 cm<sup>-1</sup>) are obtained from chemical activation.

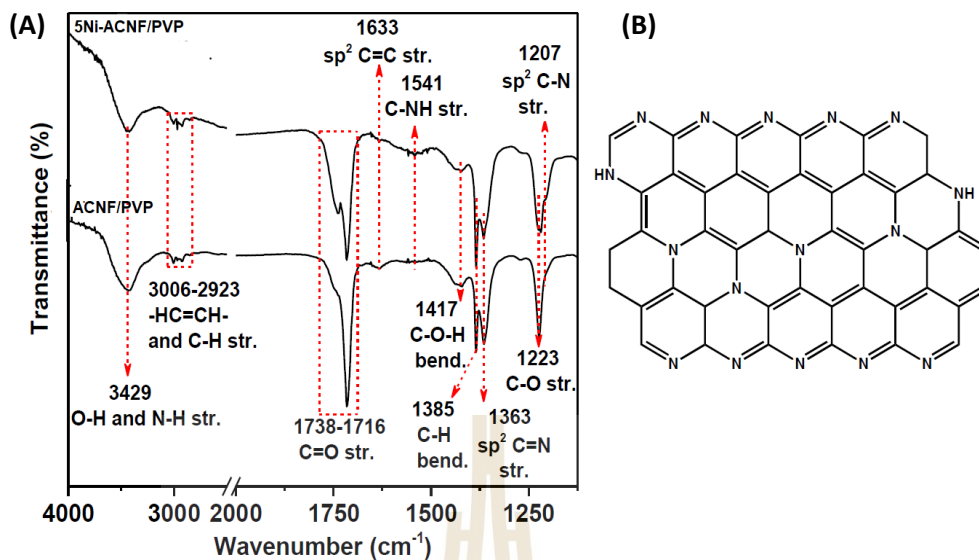


**Figure 4.9** FTIR spectra of ACNF-PVP and 5Ni-ACNF-PVP (A) and Chemical structure of PAN-based carbon nanofibers (B).

Furthermore, the surface properties and the interactions between ACNF-PVP and Ni nanoparticles are confirmed by XPS technique. From Figure 4.10(A), C 1s XPS spectrum of 5Ni-ACNF-PVP consists of C=C and C-C (284.2 eV), C-N, C=N, and C=OH (285.8 eV), and C=O (288.0 eV) (Wang et al., 2020, Wang et al., 2013, and Liu et al., 2014). These peaks correspond to the functional groups of ACNF-PVP and 5Ni-ACNF-PVP also detected in FTIR results (Figure 4.9(A)). For O 1s XPS spectra (Figure 4.10 (B)), the binding energy at 530, 531.5, and 533.3 eV correspond to the characteristic peaks of C-O-Ni, C=O and Ni-O, C-OH, and C-O-C, respectively (Liu et al., 2014 and Zhou et al., 2012). Ni 2p XPS spectrum consists of Ni-N bonds (854.3 and 871.7 eV) and Ni-O bonds (856.2 and 873.3 eV) (Li et al., 2017 and Shalom et al., 2015) (Figure 4.10 (C)). The signals of Ni-N and Ni-O bonds (Ni 2p XPS) as well as C-O-Ni (O 1s XPS) suggest the interaction between Ni nanoparticles with N and O

atoms of ACNF-PVP, while Ni-O bond also agrees with NiO. From the previous works (Vinayan et al., 2013, Zhao et al., 2019, and Shalom et al., 2015), the incorporation of heteroatoms (e.g. N and B) into supporting materials (graphene) could enhance binding energy between metal nanoparticles and supporting materials. Heteroatoms act as anchoring sites for the deposition of metal atoms, leading to the uniform distribution of metal nanoparticles on the carbon surface. Thus, the interaction between Ni nanoparticles and N atoms as well as suitable Ni loading content in this study lead to good dispersion of Ni nanoparticles, benefiting to the hydrogen adsorption of 5Ni-ACNF-PVP.

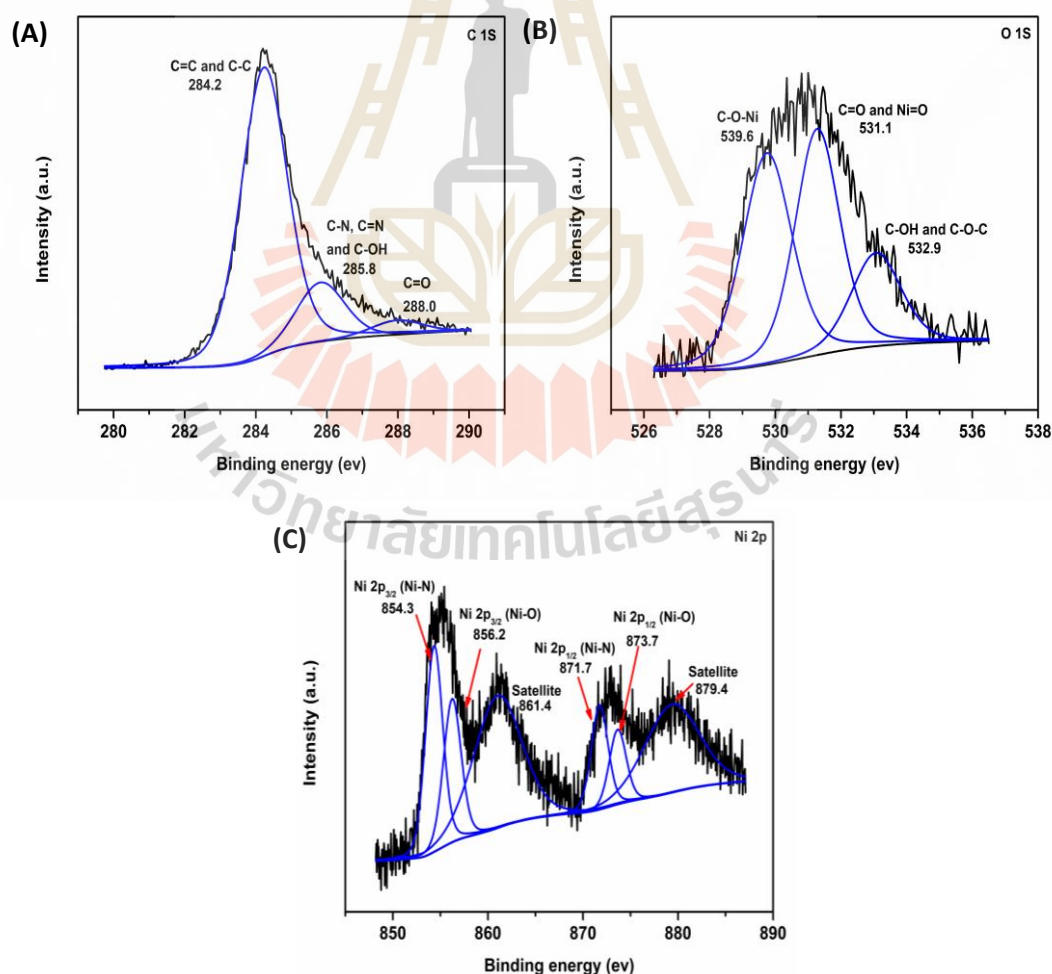


**Figure 4.10** C 1s (A), O 1s (B), and Ni 2p (C) XPS spectra of 5Ni-ACNF-PVP.

In situ x-ray absorption spectroscopy (XAS) was carried out to study the local coordination environments of Ni atoms in 5Ni-ACNF-PVP sample during reduction and hydrogen ad/desorption. Ni K-edge x-ray absorption near-edge structure (XANES) spectra of Ni-containing materials revealed the adsorption edge at ~8345 eV of electron transition from 1s to 4p orbital and the main absorption peak (the strong white line) at ~8340 eV (Anspoks et al., 2011). Prior to measuring hydrogen ad/desorption cycles, NiO in 5Ni-ACNF-PVP sample is reduced by heating to 450 °C under H<sub>2</sub> flow rate of 24 mL/min. By increasing reduction temperature, the energy of edge peak and white line intensity decreases (Figure 4.11(A)). At 450 °C, Ni K-edge XANES spectrum of 5Ni-ACNF-PVP shows comparable features to that of metallic Ni (Ni foil). This indicates successful reduction of NiO (Ni<sup>2+</sup>) to metallic Ni (Ni<sup>0</sup>) (Huang et al., 2018). Afterward, hydrogen ad/desorption cycles of 5Ni-ACNF-PVP are studied as show Figure 4.11(B). For hydrogen adsorption, the sample is cooled to room temperature (30 °C) under 24 mL H<sub>2</sub>/min and dwelled at 30 °C for 30 min. Desorption is carried out by heating the adsorbed sample to 200 °C. During hydrogen adsorption, the binding energy of edge peak and absorption edge are constant. This indicates that the local structure and oxidation state of metallic Ni are unchanged (Figure 4.11 (B)). However, the increment of absorption edge intensity is found (inset of Figure 4.11(B)), suggesting the reduction of electron occupation of Ni atoms. This implies electron transfer from Ni to hydrogen during adsorption because hydrogen has more electronegativity than Ni. In the case of hydrogen desorption, the reduction of absorption edge intensity is observed, hinting at the increase of electron occupation of Ni atoms. By cooling the desorbed 5Ni-ACNF-PVP to 30 °C, the increase of

absorption edge intensity is recovered (inset in Figure 4.11 (B)), indicating the reversibility of 5Ni-ACNF-PVP.

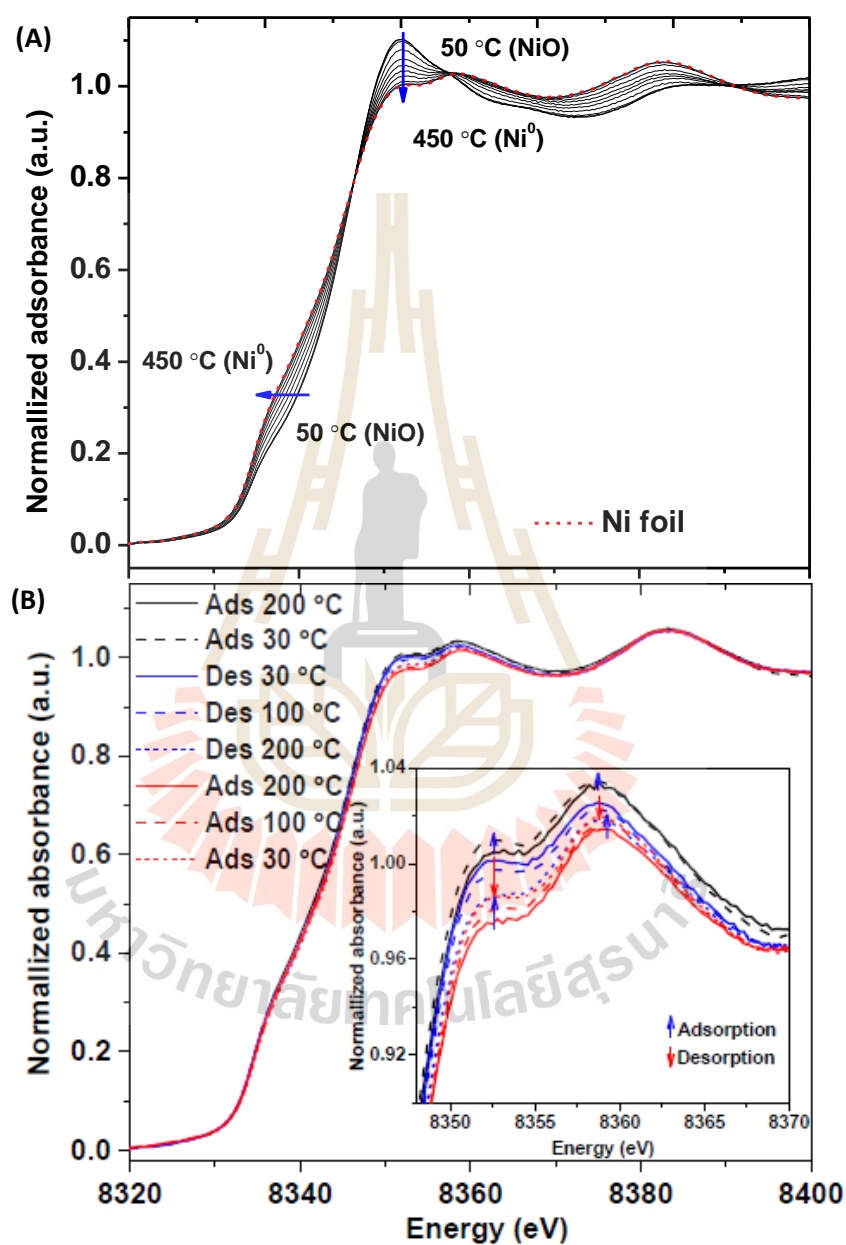


**Figure 4.11** In situ Ni K-edge XANES spectra during reduction (A) and hydrogen ad/desorption (B) of 5Ni-ACNF-PVP.

#### 4.4. Computations: Ni-N and Ni-carbon interactions

To explain the behavior of hydrogen adsorption in Ni-doped ACNF-PVP sample, the electronic structures and adsorption energy were proposed by a first-principle calculation based on DFT. The pristine graphene sheet is used as a carbon structure model. From the experimental observations, ACNF-PVP contains both graphitic lattice and disordered  $sp^3$  carbons as well as non-negligible nitrogen contents are evidenced by FTIR and XPS results (Figures 4.9(A) and 4.10(C)). Pyrrolic defect represents nitrogen heteroatoms in the carbon structure. Ni nanoparticles are represented by icosahedral  $Ni_{13}$  cluster, placed onto the vacancy of pyrrolic graphene model. From Figure 4.12(A), the optimized structure reveals that the Ni atom bonds with three N atoms. The Ni–N bond distance is averagely of 1.89 Å. This configuration corresponds to Ni–N bond observed from Ni 2p XPS spectrum (Figure 4.10(C)). The binding energy ( $E_b$ ) of the  $Ni_{13}$  cluster on the pyrrolic graphene can be calculated as follow:

$$E_b = (E_{GP} + E_{Ni_{13}}) - E_{Ni-GP} \quad (4)$$

where  $E_{GP}$  is the total energy of the bare pyrrolic graphene,  $E_{Ni_{13}}$  is the total energy of the isolated  $Ni_{13}$  cluster, and  $E_{Ni-GP}$  is the total energy of the  $Ni_{13}$  on the pyrrolic graphene system.

From computations  $E_b$  of the  $Ni_{13}$  cluster on the pyrrolic graphene is 826 kJ/mol. From the previous works, the  $E_b$  of different metal clusters supported on N-doped graphene were 735 and 804 kJ/mol for  $Ag_8$  and  $Pt_{14}$ , respectively (Tian et al., 2015

and Jalili et al., 2017). The Ni<sub>13</sub> cluster on the pyrrolic graphene has high binding energy, implying the strong interaction between Ni<sub>13</sub> cluster and pyrrolic graphene. From Figure 4.12 (A)), Bader charge analysis reveals that Ni cluster gives electrons to the support (-1.98 e<sup>-</sup>). These electrons mainly locate at the relatively high electronegative N atoms (+1.68 e<sup>-</sup>), while small fractions (+0.30 e<sup>-</sup>) are delocalized throughout the graphene sheet. The calculation suggests strong bonding between Ni particles and N-doped ACNF-PVP surface, preventing particle agglomerate upon ad/desorption cycles.

Moreover, the behavior of H<sub>2</sub> adsorption is examined using AIMD simulations, where 20 H<sub>2</sub> molecules are included in an NVT canonical ensemble at 300 K for 10 ps. From Figure 4.12 (B), dissociative adsorption of H<sub>2</sub> molecules on the Ni<sub>13</sub> cluster is observed without strong interaction between H<sub>2</sub> molecules and the graphene. Low energy configuration is selected to optimize the static structure using the DFT method. From the computation, the optimized structure contains 20 H atoms (10 H<sub>2</sub> molecules) adsorbed on the interstitial and top sites of the Ni<sub>13</sub> cluster. The adsorption energy per H<sub>2</sub> molecule (E<sub>ads</sub>) can be calculated as in equation (5).

$$E_{\text{ads}} = [E_{\text{H}_2+\text{Ni}_{13}/\text{GP}} - (n_{\text{H}_2}E_{\text{H}_2} + E_{\text{Ni}_{13}/\text{GP}})]/n_{\text{H}_2} \quad (5)$$

where E<sub>H<sub>2</sub>+Ni<sub>13</sub>/GP</sub> and E<sub>Ni<sub>13</sub>/GP</sub> are the total energies of the systems with and without H<sub>2</sub> adsorption, respectively, and E<sub>H<sub>2</sub></sub> is the total energy of a H<sub>2</sub> molecule in gas phase.

From the calculation adsorption energy, E<sub>ads</sub> is -88 kJ/mol H<sub>2</sub> with average Ni–H bond distance of 1.71 Å. This E<sub>b</sub> indicates strong chemisorption character, which slightly

affects the local structure of the Ni<sub>13</sub> cluster by elongating the Ni–Ni bond distance up to 36 pm as compared with the cluster without H<sub>2</sub> adsorption. From the previous work, calculated adsorption energy of 100-149 kJ/mol are obtained from Ni<sub>13</sub> and Pd<sub>6</sub> clusters on graphene and Pt<sub>4</sub> cluster on N-doped graphene (Roncancio S et al., 2018, Cabria et al., 2012, and Chen et al., 2018). These calculated adsorption energies of -88 kJ/mol are consistent with H<sub>2</sub> adsorption energy previously reported, but it has considerably higher than optimal values from the experiments (15-25 kJ/mol). This can be due to the fact the calculated adsorption energies are microscopic properties considering only dissociative hydrogen adsorption on Ni clusters, which molecular physisorption on the surface of active carbons are not taken into account. To approach the bonding character of the adsorbed hydrogen upon adsorption, the Bader charge analysis is carried out. Upon adsorption, the number of electrons of the Ni<sub>13</sub> cluster are depleted by 2.63 e<sup>-</sup>, while those of adsorbed hydrogen atoms enhance to +2.60 e<sup>-</sup>. The calculated results are consistent with the commonly known character of metal-hydrogen bonds, where metal usually shares its electrons with hydrogen.

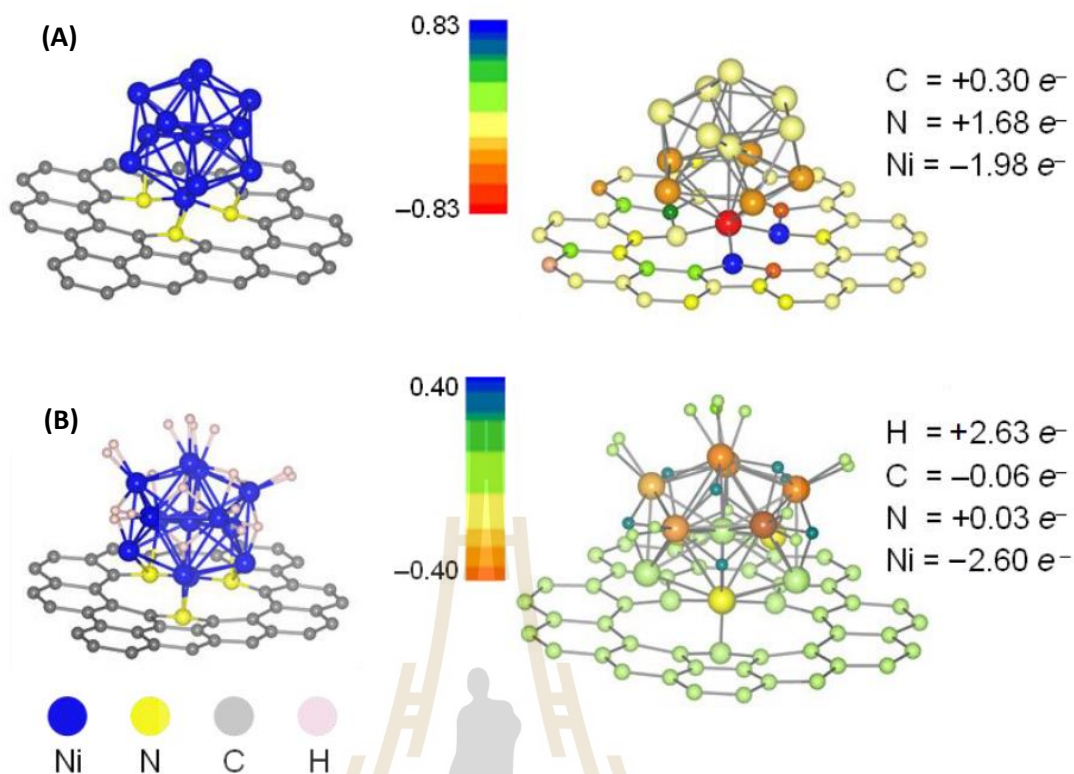


**Figure 4.12** The optimized structures of Ni<sub>13</sub> cluster on pyrrolic graphene in the absence (A) and presence (B) of hydrogen adsorption.

To confirm the behavior of charge transfer, Ni *K*-edge XANES spectra of different hydrogen coverages on Ni supported pyrrolic graphene are simulated and compared with the experimental results. The XANES spectra are simulated from the Ni atoms at the center of Ni<sub>13</sub> cluster. Ni *K*-edge XANES spectra from simulation and experiment (Figure 4.13) show two peaks at low and high energy (P1 and P2, respectively). The energy at P1 peaks of both simulation and experiment are comparable, while that of P2 shifts ~ 6 eV. From Figure 4.13, the peak intensity ratio of P1:P2 in the simulated spectra is opposite from the experimental spectrum due to the small amount of hydrogen during the experiment (24 mL H<sub>2</sub>/min). The absorption edge intensity (P1 peak) increases with hydrogen coverage (8H to 20H atoms),

indicating the reduction of occupation number of Ni cluster. This suggests electron transfer from Ni cluster to the adsorbed hydrogen. Therefore, simulated Ni K-edge XANES spectra are not only considerably in agreement with the experiment but also correspondence to the Bader charge analysis that Ni tends to share its electrons with H to form Ni–H bonds upon hydrogen adsorption. Moreover, the experiments and computations results suggest that hydrogen adsorption mechanisms of 5Ni-ACNF-PVP include not only chemisorption onto Ni nanoparticles but also physisorption and spillover of hydrogen. This proposed mechanism agrees with some calculations, suggesting that spillover was thermodynamically and kinetically difficult due to considerably high energy barrier for hydrogen migration from transition metal nanoparticles to the surface of adsorbent. Therefore, hydrogen adsorption performances can be improved by the enhanced reactive surface area and uniform distribution of Ni nanoparticles on carbon surface.

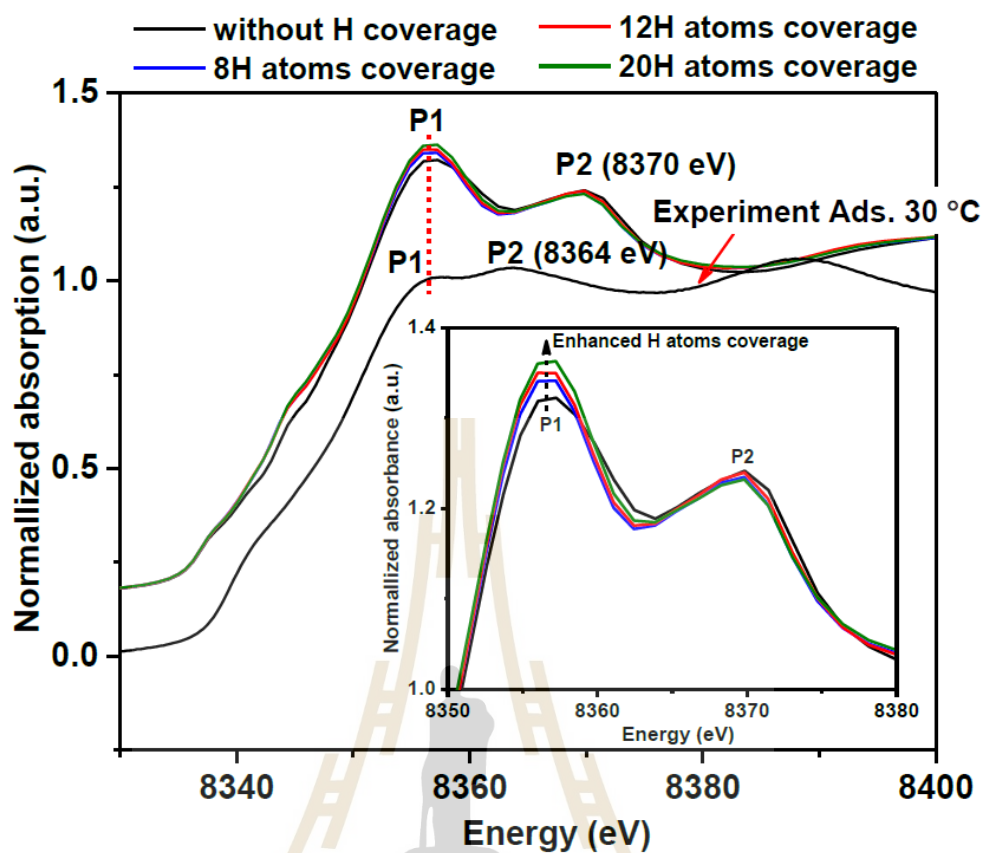


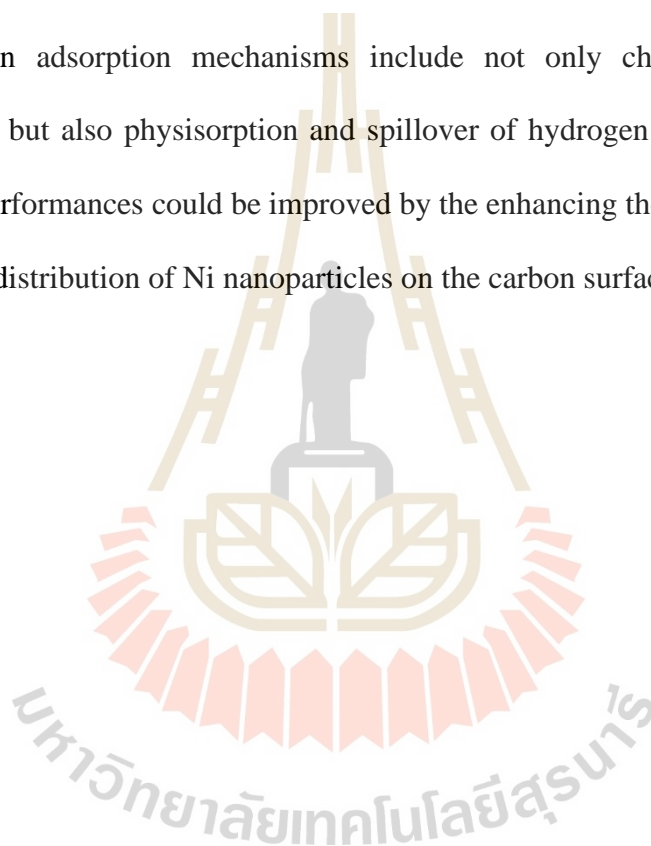
**Figure 4.13** The electron transfer is schematically depicted by the colors of each atom where the positive and negative values describe electron gains and losses, respectively. The labelled numbers represent the total number of electrons gain/loss by each atomic species. The H adsorbed structures at various hydrogen coverages are used to simulate XANES spectra as compared with the experiment.

## CHAPTER V

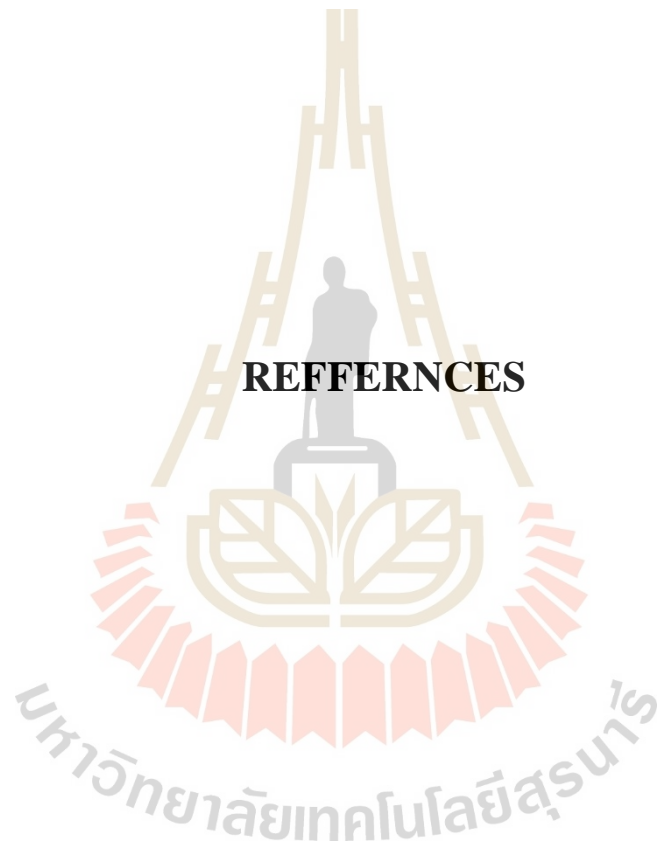
### CONCLUSIONS

Activated carbon nanofibers (ACNF-PVP) prepared by carbonization and chemical activation of electrospun polyacrylonitrile (PAN)-polyvinylpyrrolidone (PVP) were studied for hydrogen adsorption at ambient temperature. ACNF-PVP was doped with 5-20 wt. % Ni by a wet impregnation method. ACNF-PVP doped with 5 wt. % Ni revealed uniform distribution and small sizes (5-10 nm) of Ni nanoparticles, while particle agglomeration was found in ACNF-PVP loading with higher Ni contents, especially 20 wt. % Ni. Specific surface area and pore volume of ACNF-PVP were slightly decreased after doping with 5 wt. % Ni. The highest hydrogen adsorption capacity under 50 bar  $H_2$  was obtained from 5 wt. % Ni-doped ACNF-PVP (1.33 wt. %  $H_2$ ) as compared with the other samples with higher Ni loading contents (0.40-0.44 wt. %  $H_2$ ). Due to the excellent performances of 5 wt. % Ni-doped ACNF-PVP, further studies including ad/desorption under various pressures and reversibility, as well as investigation of adsorption mechanisms were carried out only on this sample. The adsorption capacity of 0.55-2.12 wt. %  $H_2$  ( $p(H_2) = 20-100$  bar) and cycling stability upon 10 cycles with average capacity of 1.17 wt. %  $H_2$  ( $p(H_2) = 50$  bar) were achieved. Ni 2p XPS spectrum and computations showed strong binding energy between Ni nanoparticles and N doped-ACNF-PVP up to 826 KJ/mol. The latter enhanced reactive surface area for hydrogen dissociative adsorption

and prevented agglomeration of Ni particles upon cycling. The calculated adsorption energies (-88 kJ/mol) were considerably higher than optimal values from the experiments (15-25 kJ/mol) since the calculated adsorption energies were microscopic properties, considering only dissociative hydrogen adsorption on Ni clusters. Both experimental and simulated XANES spectra confirmed that Ni shared its electrons to H to form Ni-H bonds with strong chemisorption character. Moreover, it was found that hydrogen adsorption mechanisms include not only chemisorption onto Ni nanoparticles but also physisorption and spillover of hydrogen. Therefore, hydrogen adsorption performances could be improved by the enhancing the reactive surface area and uniform distribution of Ni nanoparticles on the carbon surface.



**REFERENCES**



## REFERNCES

- Abdalla, A.M., Hossain, S., Nisfindy, O.B., Azad, A.T., Dawood, M. and Azad, A.K. (2018). Hydrogen production, storage, transportation and key challenges with applications: A review. **Energy conversion and management**. 165: 602-627.
- Amaya-Roncancio, S., Blanco, A.G., Linares, D.H. and Sapag, K. (2018). DFT study of hydrogen adsorption on Ni/graphene. **Applied Surface Science**. 447: 254-260.
- Anspoks, A. and Kuzmin, A. (2011). Interpretation of the Ni K-edge EXAFS in nanocrystalline nickel oxide using molecular dynamics simulations. **Journal of Non-crystalline Solids**. 357: 2604-2610.
- Ariharan, A., Viswanathan, B. and Nandhakumar, V. (2017). Nitrogen doped graphene as potential material for hydrogen storage. **Graphene**. 6(2): 41-60.
- Banerjee, S., Dasgupta, K., Kumar, A., Ruz, P., Vishwanadh, B., Joshi, J. and Sudarsan, V. (2015). Comparative evaluation of hydrogen storage behavior of Pd doped carbon nanotubes prepared by wet impregnation and polyol methods. **International Journal of Hydrogen Energy**. 40(8): 3268-3276.
- Bognitzki, M., Frese, T., Steinhart, M., Greiner, A., Wendorff, J.H., Schaper, A. and Hellwig, M. (2001). Preparation of fibers with nanoscaled morphologies: electrospinning of polymer blends. **Polymer Engineering & Science**. 41(6): 982-989.

- Cabria, I., López, M., Fraile, S. and Alonso, J. (2012). Adsorption and dissociation of molecular hydrogen on palladium clusters supported on graphene. **The Journal of Physical Chemistry C**. 116(40): 21179-21189.
- Chaves, A.S., Piotrowski, M.J. and Da Silva, J.L. (2017). Evolution of the structural, energetic, and electronic properties of the 3d, 4d, and 5d transition-metal clusters (30 TM  $n$  systems for  $n= 2-15$ ): a density functional theory investigation. **Physical Chemistry Chemical Physics**. 19(23): 15484-15502.
- Chen, I.-N., Wu, S.-Y. and Chen, H.-T. (2018). Hydrogen storage in N-and B-doped graphene decorated by small platinum clusters: A computational study. **Applied Surface Science**. 441: 607-612.
- Chen, Y. and Liu, Y. (2014). Preparation of porous carbon with high dispersion of Ru nanoparticles by sol-gel method and its application in hydrogen storage. **Journal of Materials Chemistry A**. 2(24): 9193-9199.
- Choi, D.I., Lee, J.-N., Song, J., Kang, P.-H., Park, J.-K. and Lee, Y.M. (2013). Fabrication of polyacrylonitrile/lignin-based carbon nanofibers for high-power lithium ion battery anodes. **Journal of Solid State Electrochemistry**. 17(9): 2471-2475.
- Cuesta, A., Dhamelinourt, P., Laureyns, J., Martinez-Alonso, A. and Tascón, J.D. (1994). Raman microprobe studies on carbon materials. **Carbon**. 32(8): 1523-1532.
- Divya, P. and Ramaprabhu, S. (2014). Hydrogen storage in platinum decorated hydrogen exfoliated graphene sheets by spillover mechanism. **Physical Chemistry Chemical Physics**. 16(48): 26725-26729.

- Elyassi, M., Rashidi, A., Hantehzadeh, M.R. and Elahi, S.M. (2017). Preparation of different graphene nanostructures for hydrogen adsorption. **Surface and Interface Analysis**. 49(4): 230-237.
- Eren, O., Ucar, N., Onen, A., Kizildag, N. and Karacan, I. (2016). Synergistic effect of polyaniline, nanosilver, and carbon nanotube mixtures on the structure and properties of polyacrylonitrile composite nanofiber. **Journal of Composite Materials**. 50(15): 2073-2086.
- Geng, Z., Wang, D., Zhang, C., Zhou, X., Xin, H., Liu, X. and Cai, M. (2014). Spillover enhanced hydrogen uptake of Pt/Pd doped corncob-derived activated carbon with ultra-high surface area at high pressure. **International Journal of Hydrogen Energy**. 39(25): 13643-13649.
- Grimme, S. (2006). Semiempirical GGA-type density functional constructed with a long-range dispersion correction. **Journal of computational chemistry**. 27(15): 1787-1799.
- Grimme, S., Antony, J., Ehrlich, S. and Krieg, H. (2010). A consistent and accurate ab initio parametrization of density functional dispersion correction (DFT-D) for the 94 elements H-Pu. **The Journal of chemical physics**. 132(15): 154104.
- Han, Y.-J. and Park, S.-J. (2017). Influence of nickel nanoparticles on hydrogen storage behaviors of MWCNTs. **Applied Surface Science**. 415: 85-89.
- Hedin, L. and Lundqvist, B.I. (1971). Explicit local exchange-correlation potentials. **Journal of Physics C: Solid state physics**. 4(14): 2064.
- Huang, C.-C., Li, Y.-H., Wang, Y.-W. and Chen, C.-H. (2013). Hydrogen storage in cobalt-embedded ordered mesoporous carbon. **International Journal of Hydrogen Energy**. 38(10): 3994-4002.

- Huang, L., Yan, L., Tang, M., Wang, G., Qin, Z. and Ge, H. (2018). Effect of pretreatment on the adsorption performance of Ni/ZnO adsorbent for dibenzothiophene desulfurization. **ACS omega**. 3(12): 18967-18975.
- Ibupoto, A.S., Qureshi, U.A., Ahmed, F., Khatri, Z., Khatri, M., Maqsood, M., Brohi, R.Z. and Kim, I.S. (2018). Reusable carbon nanofibers for efficient removal of methylene blue from aqueous solution. **Chemical Engineering Research and Design**. 136: 744-752.
- Im, J.S., Park, S.-J., Kim, T.J., Kim, Y.H. and Lee, Y.-S. (2008). The study of controlling pore size on electrospun carbon nanofibers for hydrogen adsorption. **Journal of colloid and interface science**. 318(1): 42-49.
- Jalili, S., Goliaei, E.M. and Schofield, J. (2017). Silver cluster supported on nitrogen-doped graphene as an electrocatalyst with high activity and stability for oxygen reduction reaction. **International Journal of Hydrogen Energy**. 42(21): 14522-14533.
- Jawhari, T., Roid, A. and Casado, J. (1995). Raman spectroscopic characterization of some commercially available carbon black materials. **Carbon**. 33(11): 1561-1565.
- Jiménez, V., Sánchez, P., Díaz, J.A., Valverde, J.L. and Romero, A. (2010). Hydrogen storage capacity on different carbon materials. **Chemical Physics Letters**. 485(1-3): 152-155.
- Jin, H., Lee, Y.S. and Hong, I. (2007). Hydrogen adsorption characteristics of activated carbon. **Catalysis today**. 120(3-4): 399-406.
- Kang, K.Y., Lee, B.I. and Lee, J.S. (2009). Hydrogen adsorption on nitrogen-doped carbon xerogels. **Carbon**. 47(4): 1171-1180.

- Kaskun, S. and Kayfeci, M. (2018). The synthesized nickel-doped multi-walled carbon nanotubes for hydrogen storage under moderate pressures. **International Journal of Hydrogen Energy**. 43(23): 10773-10778.
- Kim, B.-J., Lee, Y.-S. and Park, S.-J. (2008). A study on the hydrogen storage capacity of Ni-plated porous carbon nanofibers. **International Journal of Hydrogen Energy**. 33(15): 4112-4115.
- Kim, B.-J. and Park, S.-J. (2007). Influence of surface treatments on micropore structure and hydrogen adsorption behavior of nanoporous carbons. **Journal of colloid and interface science**. 311(2): 619-621.
- Kim, O.-H., Cho, Y.-H., Chung, D.Y., Kim, M.J., Yoo, J.M., Park, J.E., Choe, H. and Sung, Y.-E. (2015). Facile and gram-scale synthesis of metal-free catalysts: toward realistic applications for fuel cells. **Scientific reports**. 5(1): 1-8.
- Kresse, G. and Furthmüller, J. (1996). Efficiency of ab-initio total energy calculations for metals and semiconductors using a plane-wave basis set. **Computational materials science**. 6(1): 15-50.
- Kresse, G. and Joubert, D. (1999). From ultrasoft pseudopotentials to the projector augmented-wave method. **Physical review b**. 59(3): 1758.
- Kuchta, B., Firlej, L., Roszak, S. and Pfeifer, P. (2010). A review of boron enhanced nanoporous carbons for hydrogen adsorption: numerical perspective. **Adsorption**. 16(4-5): 413-421.
- Langmi, H.W., Ren, J., North, B., Mathe, M. and Bessarabov, D. (2014). Hydrogen storage in metal-organic frameworks: a review. **Electrochimica Acta**. 128: 368-392.

- Larminie, J., Dicks, A. and McDonald, M.S. (2003). Fuel cell systems explained, **J. Wiley Chichester, UK.**
- Lastoskie, C., Gubbins, K.E. and Quirke, N. (1993). Pore size distribution analysis of microporous carbons: a density functional theory approach. **The journal of physical chemistry.** 97(18): 4786-4796.
- Lee, Y.S., Kim, Y.H., Hong, J.S., Suh, J.K. and Cho, G.J. (2007). The adsorption properties of surface modified activated carbon fibers for hydrogen storages. **Catalysis today.** 120(3-4): 420-425.
- Li, B., Nam, H., Zhao, J., Chang, J., Lingappan, N., Yao, F., Lee, T.H. and Lee, Y.H. (2017). Nanoreactor of Nickel-Containing Carbon-Shells as Oxygen Reduction Catalyst. **Advanced materials.** 29(7): 1605083.
- Li, Y. and Yang, R.T. (2006). Hydrogen storage in metal-organic frameworks by bridged hydrogen spillover. **Journal of the American Chemical Society.** 128(25): 8136-8137.
- Lin, K.-Y., Tsai, W.-T. and Chang, J.-K. (2010). Decorating carbon nanotubes with Ni particles using an electroless deposition technique for hydrogen storage applications. **International Journal of Hydrogen Energy.** 35(14): 7555-7562.
- Lin, Z., Chen, X., Yin, C., Tang, H., Hu, Y. and Ning, X. (2011). Theoretical prediction of the growth and surface structure of Pt and Ni nanoparticles. **EPL (Europhysics Letters).** 96(6): 66005.
- Liu, H., Kuila, T., Kim, N.H., Ku, B.-C. and Lee, J.H. (2013). In situ synthesis of the reduced graphene oxide-polyethyleneimine composite and its gas barrier properties. **Journal of Materials Chemistry A.** 1(11): 3739-3746.

- Liu, J., Lv, W., Wei, W., Zhang, C., Li, Z., Li, B., Kang, F. and Yang, Q.-H. (2014). A three-dimensional graphene skeleton as a fast electron and ion transport network for electrochemical applications. **Journal of Materials Chemistry A**. 2(9): 3031-3037.
- Liu, X., Li, S., Mei, J., Lau, W.-M., Mi, R., Li, Y., Liu, H. and Liu, L. (2014). From melamine–resorcinol–formaldehyde to nitrogen-doped carbon xerogels with micro-and meso-pores for lithium batteries. **Journal of Materials Chemistry A**. 2(35): 14429-14438.
- Monkhorst, H.J. and Pack, J.D. (1976). Special points for Brillouin-zone integrations. **Physical review b**. 13(12): 5188.
- Nosé, S. (1984). A molecular dynamics method for simulations in the canonical ensemble. **Molecular physics**. 52(2): 255-268.
- Pang, Q., Tang, J., Huang, H., Liang, X., Hart, C., Tam, K.C. and Nazar, L.F. (2015). A nitrogen and sulfur dual-doped carbon derived from Polyrhodanine@ Cellulose for advanced lithium–sulfur batteries. **Advanced materials**. 27(39): 6021-6028.
- Park, S., Kim, B., Lee, Y., and Cho, M. (2008). Influence of copper electroplating on high pressure hydrogen-storage behaviors of activated carbon fibers. **International Journal of Hydrogen Energy**. 33: 1707-1710.
- Perdew, J.P., Burke, K. and Ernzerhof, M. (1996). Generalized gradient approximation made simple. **Physical review letters**. 77(18): 3865.
- Pollet, B.G., Staffell, I. and Shang, J.L. (2012). Current status of hybrid, battery and fuel cell electric vehicles: From electrochemistry to market prospects. **Electrochimica Acta**. 84: 235-249.

- Rangel, E., Sansores, E., Vallejo, E., Hernández-Hernández, A. and López-Pérez, P. (2016). Study of the interplay between N-graphene defects and small Pd clusters for enhanced hydrogen storage via a spill-over mechanism. **Physical Chemistry Chemical Physics**. 18(48): 33158-33170.
- Rehr, J.J., Kas, J.J., Prange, M.P., Sorini, A.P., Takimoto, Y. and Vila, F. (2009). Ab initio theory and calculations of X-ray spectra. **Comptes Rendus Physique**. 10(6): 548-559.
- Roberts, A.D., Wang, S., Li, X. and Zhang, H. (2014). Hierarchical porous nitrogen-rich carbon monoliths via ice-templating: high capacity and high-rate performance as lithium-ion battery anode materials. **Journal of Materials Chemistry A**. 2(42): 17787-17796.
- Sawant, S.V., Banerjee, S., Patwardhan, A.W., Joshi, J.B. and Dasgupta, K. (2020). Synthesis of boron and nitrogen co-doped carbon nanotubes and their application in hydrogen storage. **International Journal of Hydrogen Energy**. 45(24): 13406-13413.
- Shafiee, S. and Topal, E. (2009). When will fossil fuel reserves be diminished? **Energy policy**. 37(1): 181-189.
- Shalom, M., Ressnig, D., Yang, X., Clavel, G., Fellingner, T.P. and Antonietti, M. (2015). Nickel nitride as an efficient electrocatalyst for water splitting. **Journal of Materials Chemistry A**. 3(15): 8171-8177.
- Ströbel, R., Garche, J., Moseley, P., Jörissen, L. and Wolf, G. (2006). Hydrogen storage by carbon materials. **Journal of power sources**. 159(2): 781-801.
- Tian, Y., Liu, Y.-j., Zhao, J.-x. and Ding, Y.-h. (2015). High stability and superior catalytic reactivity of nitrogen-doped graphene supporting Pt nanoparticles as

a catalyst for the oxygen reduction reaction: a density functional theory study.

**RSC advances.** 5(43): 34070-34077.

Toyota's Strategy for Environmental Technologies.

[http://www.toyota.com.cn/innovation/environmental\\_technology/strategy\\_environmental\\_tech.html](http://www.toyota.com.cn/innovation/environmental_technology/strategy_environmental_tech.html). [On-line].

U. S. Department of Energy. (2017). Materials-Based Hydrogen Storage. [On-line].

Vinayan, B., Sethupathi, K. and Ramaprabhu, S. (2013). Facile synthesis of triangular shaped palladium nanoparticles decorated nitrogen doped graphene and their catalytic study for renewable energy applications. **International Journal of Hydrogen Energy.** 38(5): 2240-2250.

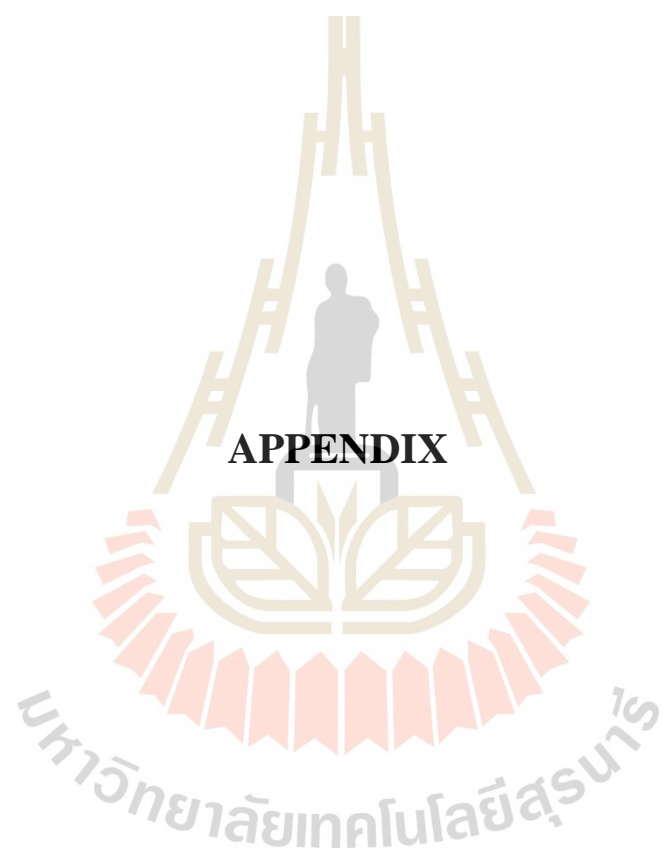
Wang, R., Wang, Y., Xu, C., Sun, J. and Gao, L. (2013). Facile one-step hydrazine-assisted solvothermal synthesis of nitrogen-doped reduced graphene oxide: reduction effect and mechanisms. **RSC advances.** 3(4): 1194-1200.

Wang, X., Wu, D., Dai, C., Xu, C., Sui, P., Feng, R., Wei, Y., Fu, X.-Z. and Luo, J.-L. (2020). Novel folic acid complex derived nitrogen and nickel co-doped carbon nanotubes with embedded Ni nanoparticles as efficient electrocatalysts for CO<sub>2</sub> reduction. **Journal of Materials Chemistry A.** 8(10): 5105-5114.

Xia, K., Hu, J. and Jiang, J. (2014). Enhanced room-temperature hydrogen storage in super-activated carbons: The role of porosity development by activation. **Applied Surface Science.** 315: 261-267.

Ya'aini, N., Pillay, A., Krishnan, L.G. and Ripin, A. (2019). Synthesis of activated carbon doped with transition metals for hydrogen storage. **EDP Sciences.** 90: 01016.

- Yadav, A., Faisal, M., Subramaniam, A. and Verma, N. (2017). Nickel nanoparticle-doped and steam-modified multiscale structure of carbon micro-nanofibers for hydrogen storage: effects of metal, surface texture and operating conditions. **International Journal of Hydrogen Energy**. 42(9): 6104-6117.
- Yang, R.T. and Wang, Y. (2009). Catalyzed hydrogen spillover for hydrogen storage. **Journal of the American Chemical Society**. 131(12): 4224-4226.
- Zhao, W., Fierro, V., Zlotea, C., Izquierdo, M., Chevalier-César, C., Latroche, M. and Celzard, A. (2012). Activated carbons doped with Pd nanoparticles for hydrogen storage. **International Journal of Hydrogen Energy**. 37(6): 5072-5080.
- Zhao, W., Luo, L., Chen, T., Li, Z., Zhang, Z., Wang, H., Rao, J., Feo, L. and Fan, M. (2019). Synthesis and characterization of Pt-N-doped activated biocarbon composites for hydrogen storage. *Composites Part B: Engineering*. 161: 464-472.
- Zhou, G., Wang, D.-W., Yin, L.-C., Li, N., Li, F. and Cheng, H.-M. (2012). Oxygen bridges between NiO nanosheets and graphene for improvement of lithium storage. **ACS nano**. 6(4): 3214-3223.



## APPENDIX

### CALCULATION FOR SYNTHESIS OF NICKEL DOPED

#### ACNF-PVP

##### Calculation molar ratio of Nickel: ACNF-PVP

$$(\text{Ni}(\text{NO}_3)_2 \cdot 6\text{H}_2\text{O}) \quad \text{Mw} = 290.7 \text{ gmol}^{-1}$$

$$\text{Ni} \quad \text{Mw} = 58.7 \text{ gmol}^{-1}$$

$$\text{wt. \% Ni} = [\text{Mw of } (\text{Ni}(\text{NO}_3)_2 \cdot 6\text{H}_2\text{O}) / \text{Mw of Ni}] \times \text{weigh of Ni}$$

Sample: 5Ni-ACNF-PVP

$$5 \text{ wt. \% Ni} = [290.7 \text{ gmol}^{-1} / 58.7 \text{ gmol}^{-1}] \times 0.05 \text{ g}$$

$$= 248.0 \text{ g}$$

Sample: 10Ni-ACNF-PVP

$$10 \text{ wt. \% Ni} = [290.7 \text{ gmol}^{-1} / 58.7 \text{ gmol}^{-1}] \times 0.10 \text{ g}$$

$$= 495.5 \text{ g}$$

Sample: 20Ni-ACNF-PVP

$$20 \text{ wt. \% Ni} = [290.7 \text{ gmol}^{-1} / 58.7 \text{ gmol}^{-1}] \times 0.20 \text{ g}$$

$$= 991.0 \text{ g}$$

## CALCULATION OF HYDROGER CAPACITY

Calculation of hydrogen desorption capacity of 5Ni-ACNF-PVP under 100 bar H<sub>2</sub>

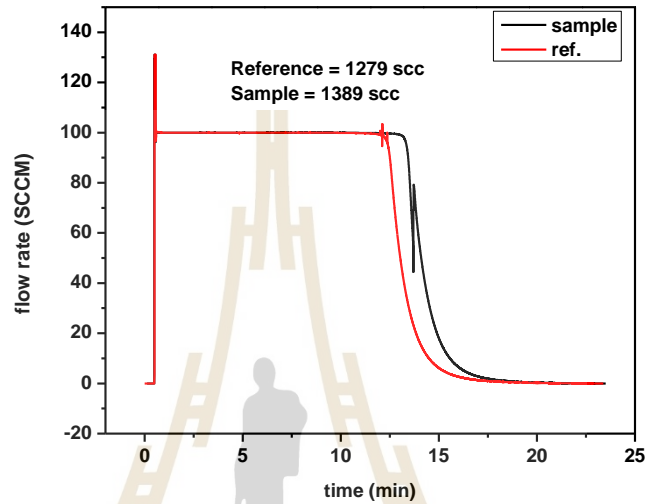


Figure A Flow rate of hydrogen desorption of sample and reference.

$$V_{STP} = \frac{P_s V_s T_{TP}}{T_s P_{STP}}$$

$$n_{H_2} = \frac{V_{STP}}{22.4 \frac{L}{mol}}$$

$$H_2 \text{ capacity (wt. \%)} = \frac{n_{H_2} \times 2.016 \frac{g}{mol}}{\text{sample weight}} \times 100$$

T<sub>s</sub> is temperature at standard condition of MFC of 294.95 K

P<sub>s</sub> is pressure at standard condition of MFC of 1.0167 bar

V<sub>s</sub> (SL) is volumes of hydrogen gas at standard condition of MFC

$V_{\text{STP}}$  (L) is volumes of hydrogen gas at standard temperature and pressure condition

(STP,  $T_{\text{STP}} = 273.15$  K and  $P_{\text{STP}} = 1.0133$  bar)

$n_{\text{H}_2}$  (mol) is hydrogen moles and standard molar volume is  $22.4 \text{ Lmol}^{-1}$

$$\text{sample mass} = 0.4341 \text{ g}$$

$$\text{Peak area} = 110 \text{ SCC}$$

$$P_s = 1.0167 \text{ bar}$$

$$V_s = 0.11 \text{ L}$$

$$T_s = 294.95 \text{ K}$$

$$T_{\text{STP}} = 273.15 \text{ K}$$

$$P_{\text{STP}} = 1.0133 \text{ bar}$$

$$V_{\text{STP}} = [1.0167 \text{ bar} \times 0.11 \text{ L} \times 273.15 \text{ K}] / [294.95 \text{ K} \times 1.0133 \text{ bar}]$$

$$= 0.1022 \text{ L}$$

$$n_{\text{H}_2} = [0.1022 \text{ L}] / [22.4 \text{ Lmol}^{-1}]$$

$$= 0.004564 \text{ mol}$$

$$\text{H}_2 \text{ capacity (wt.\%)} = [0.004564 \text{ mol} \times 2.016 \text{ Lmol}^{-1} / 0.4341 \text{ g}] \times 100$$

$$= 2.12 \text{ wt. \%}$$

# CURRICULUM VITAE

**Name** Miss Natthaporn Thaweelap

**Born** June 16<sup>st</sup>, 1994 in Buriram, Thailand

**Address** 93 Moo 1, Tambon Lumchaiyong, Amphor Nangrong, Buriram, 31110,  
Thailand

**E-mail** M5910038@g.sut.ac.th.com

## Education

2012-2015 B.Sc. (Chemistry), Suranaree University of Technology,  
Thailand

2016-present Student in M.Sc. Program in Chemistry, Suranaree  
University of Technology, Thailand

## Publications

Thaweelap N., Thongtan P., Sitthiwet Ch., Thangviriya S., Eiamlamai P., and Utke R.

(2017)<sup>1</sup> Hydrogen sorption, kinetics, reversibility, and reaction mechanisms of MgH<sub>2</sub>

-xLiBH<sub>4</sub> doped with activated carbon nanofibers for reversible hydrogen storage

based laboratory powder and tank scales. **International Journal of Hydrogen**

**Energy**. 42(39): 24915-24926. (Impact factor (2017): 2.31)